

---

# **Velocity Distribution Functions of Pickup Ions with Ulysses/SWICS**

---

MASTER THESIS

Anne Fischer  
Dezember 2019

Christian-Albrechts-Universität zu Kiel  
Institut für Experimentelle und Angewandte Physik  
Arbeitsgruppe Extraterrestrische Physik



# Abstract

Pickup ions (PUI) are former neutral atoms that are ionized in the heliosphere. The neutral atom's origin is either the interstellar medium (interstellar PUI) or a source within the heliosphere (inner-source PUI).

After ionization, the PUI's velocity distribution function (VDF) is shaped by interaction with the magnetized solar wind plasma. The general idea is that PUI are swept outwards with the solar wind and that their initially anisotropic VDF is rapidly deformed by different processes and conditions within the heliosphere. The details of involved mechanisms like e.g. pitch-angle scattering and adiabatic cooling are not completely understood to this day. A study of the evolution of the VDF helps us to understand the origin of PUI and of the underlying effects that shape the VDF.

However, most observations of PUI are limited to 1D reduced velocity measurements in the spacecraft frame. Consequently, they do not allow for interpretations without making assumptions about the underlying VDF.

In this Master thesis we want to develop a method for resolving data measured by the Solar Wind Ion Composition Spectrometer (SWICS) onboard the spacecraft Ulysses in three dimensions. SWICS is a time-of-flight mass spectrometer, that is able to determine the mass, mass-per-charge and energy of ions by independent measurements of the ion's energy-per-charge, time-of-flight and residual energy. Additionally, SWICS provides information on the inflow direction of incident ions by a three-part division of the sensor and a sectorization of Ulysses' spin. For translating this information correctly into three dimensional velocity components it is necessary to consider Ulysses' orientation in space at any time of measurement.

In this work, we utilize a virtual detector to perform a transformation from Ulysses SWICS PHA data into three dimensional velocity components on the example of He<sup>+</sup> PUI.

With this directional information a transformation from the measured absolute velocity can be performed He<sup>+</sup>! The thesis starts with an introduction into PUI, before the Ulysses mission and the instrument SWICS with its measurement principle are described. In the third chapter a virtual detector is introduced and utilized to translate the He<sup>+</sup> Pulse Height Analysis data into three dimensional velocity components. To achieve this translation, Ulysses' orientation in space and its eigen-velocity have been considered. In the final section the obtained three dimensional spectra are presented in different projections.

A virtual detector is utilized to combine absolute velocity measurements with the orientation of the instrument.



# Contents

<b>Abstract</b>	<b>iii</b>
<b>1 Pickup Ions</b>	<b>3</b>
1.1 The Heliosphere / Introduction . . . . .	3
1.2 Pickup Ions . . . . .	3
1.3 Interstellar Pickup Ions . . . . .	4
1.4 Inner-source Pickup Ions . . . . .	4
1.5 VDF . . . . .	5
1.5.1 1D reduced VDF, aim of this work...? . . . . .	7
<b>2 Instrumentation</b>	<b>9</b>
2.1 Ulysses . . . . .	9
2.2 SWICS . . . . .	10
2.2.1 Collimator and Electrostatic Analyzer . . . . .	10
2.2.2 Time-of-flight measurement . . . . .	11
2.2.3 Energy measurement . . . . .	12
2.3 Data products . . . . .	13
2.3.1 Detection Efficiency . . . . .	14
2.3.2 Priority Weighting . . . . .	15
2.4 ET matrices, identification . . . . .	16
2.4.1 Selection of He <sup>+</sup> . . . . .	17
2.4.2 Selection of He <sup>2+</sup> . . . . .	18
<b>3 Data Analysis and Methods</b>	<b>21</b>
3.1 Coordinate Systems . . . . .	21
3.1.1 Heliographic Coordinate System . . . . .	21
3.1.2 Radial Tangential Normal Coordinate System . . . . .	22
3.2 The Detector Model . . . . .	23
3.2.1 Construction . . . . .	23
From Field of View to Velocity Space . . . . .	25
3.2.2 Ulysses' Eigen-velocity . . . . .	26
3.2.3 Orientation of the Detector . . . . .	27
Calculation of the Aspect Angle . . . . .	27
Consistency Check . . . . .	29
TODO: Sunpulse Trigger – Rotation . . . . .	30
Transformation into <i>w</i> -space . . . . .	31
3.3 Velocity Distribution Function .....? . . . . .	32
3.3.1 Velocity Space Coverage . . . . .	32
3.3.2 Phase Space Normalization . . . . .	33
<b>4 Results</b>	<b>37</b>
4.1 Spherical Projection . . . . .	43
4.2 1D Projection . . . . .	46

<b>5 Summary and Outlook</b>	<b>47</b>
<b>A PSD – Sequence</b>	<b>49</b>
<b>Bibliography</b>	<b>55</b>
<b>Eidesstattliche Erklärung</b>	<b>57</b>
<b>Danksagung</b>	<b>59</b>





## Chapter 1

# Pickup Ions

Pickup ions are created when neutral atoms inside the heliosphere become ionised and are subsequently swept away with the heliospheric magnetic field that is embedded within the solar wind.

## 1.1 The Heliosphere / Introduction

Oder Überkapitel Solar Physics?

Heliosphere: Grenze zu LISM

Solar Wind: Zusammensetzung, schneller und langsamer, high latitudes: less complex, constant in speed

B-Feldgleichung

Irgendwohin muss unbedingt Motivation, warum PUIs überhaupt interessant sind zu messen!

PU Process

## 1.2 Pickup Ions

A neutral atom inside the heliosphere is only subjected to the gravitational force and radiation pressure of the sun. It is not sensitive to any electromagnetic forces until it becomes ionised by solar ultra-violet radiation, charge exchange with solar wind protons or electron impact (Q?). After ionisation the particle starts interacting with the solar wind plasma. In particular it is forced onto a gyro orbit about the heliospheric magnetic field that is embedded within the solar wind. As the freshly created ion is swept away with the magnetic field line it is “picked up” from its location of ionisation – a new pickup ion (PUI) has been created.

PUIs were first observed by Möbius et al. (1985) with the SULEICA Instrument on the AMPTE spacecraft. The particles measured at 1 AU were He<sup>+</sup> ions of interstellar origin.

Once the particle is ionised, its probability to become ionised another time decreases (Quelle). This characteristic of being only singly charged can help to discriminate PUIs from solar wind ions, that are mostly more often charged (Q?).

PUIs are mostly only single charged. This characteristic can help to distinguish them

from solar wind ions of coronal origin which often have been ionized multiple times, if not completely. (Q?)

VDF non-maxwellian, spatial density pattern

There have been observed several species of PUIs:

### 1.3 Interstellar Pickup Ions

Heliosheath, relative motion

The neutral part of the LISM can enter the heliosphere as it is not affected by the heliosheath (Todo). Inside the heliosphere the neutrals are guided only by the gravitational force and radiation pressure of the sun. The neutral particle's species determines how deep it can travel into the heliosphere before it becomes ionized. Species with a higher First Ionization Potential will be able to approach the sun much closer without being ionized. This results in He<sup>+</sup> being the dominant PUI species at a solar distance of 1 AU even if in the LISM the abundance of hydrogen is about 10 times the one of helium.

- ionisation process is also dependent on the species
- radiation pressure only important for H (and He?). Kepler orbit...
- Spatial distribution:  
gravitational force and radiation pressure lead to two regions of enhanced density of neutrals (in the ecliptic): Focusing cone and crescent. Focusing cone: For species with high FIP (as the others are ionized before and do not reach the downwind side of the sun)
- variation of He<sup>+</sup> with the solar cycle: Rucinski 2003
- H, O and N are depleted in the filtration region (Baranov Malama 1995), Wimmer Skript: even before ionization: density is determined by ratio of gravitational force and photon pressure
- neutral density determines PUI production rate

### 1.4 Inner-source Pickup Ions

The idea of an additional source for the PUI's neutral seed population was born when Geiss, Gloeckler, Fisk, et al. (1995) measured a global distribution of C<sup>+</sup> PUIs with the SWICS instrument on Ulysses. Interstellar carbon exists almost exclusively in a single charged state (Frisch et al., 2011) in the LISM. As only neutral atoms can enter the heliosphere it was not expected to find a distinct signature of C<sup>+</sup> pickup ions. However, pickup carbon was observed with about the same ratio as oxygen, of which, in contrast, 80% is in a neutral charge state in the interstellar medium. These findings suggested that there must be another source for neutrals that has its origin somewhere inside the heliosphere.

In following studies (e.g. Geiss, Gloeckler, and Steiger, 1995) there were found also other species like O<sup>+</sup> and Ne<sup>+</sup> of these, so called, inner-source PUIs.

Inner-source PUIs show a composition that is similar to the one of the solar wind

(Gloeckler et al., 2000; Allegrini et al., 2005) as well as a velocity distribution function that is centered around  $w_{SC} \approx 1$  (Schwadron et al., 2000) and seems to have thermalized with the solar wind.

Beneath those two characteristics there are other aspects concerning inner-source PUIs, that are still under debate. In particular that is the production mechanism of their neutral seed population. Allegrini et al. (2005) has summarized current candidates for possible scenarios. Two of those give an explanation for the ion's composition as they directly incorporate solar wind ions in the process:

- Solar wind recycling (Gloeckler et al., 2000; Schwadron et al., 2000): Absorption of solar wind ions by heliospheric grains and subsequent reemission of neutral atoms
- Solar wind neutralization (Wimmer-Schweingruber and Bochsler, 2002): Solar wind ions penetrate sub-micron-sized dust grains and undergo (partial) neutralization by charge exchange

(As this work does not focus on inner-source PUIs in particular...)

## 1.5 VDF

After the particle has been ionised it is forced onto a gyro motion about the local field line of the heliospheric magnetic field due to the Lorentz force.

To examine the velocity distribution of PUIs after they have been ionized we need to consider the initial speed  $v_{ini}$  of the neutral particle. For neutrals from the LISM this is mainly given by the inflow speed  $v_{ISM}$  of the local interstellar medium with which they enter the heliosphere. As we don't exactly know about the production mechanism of inner-source PUIs, the following considerations mainly relate to interstellar PUIs. Schwadron et al. (2015) obtained  $v_{ISM} \approx 25 \text{ km s}^{-1}$  with the IBEX satellite for helium. Considering the acceleration by the sun's gravitational force we have a maximum initial speed of  $v_{ini} \approx 50 \text{ km s}^{-1}$  at 1 AU. Compared to an average solar wind speed of  $v_{sw} \approx 400 \text{ km s}^{-1}$  one can neglect this initial speed in a first step.

For simplicity we thus consider a neutral particle at rest that becomes ionized by one of the aforementioned processes. The freshly created ion now is subjected to the electromagnetic forces of the solar wind plasma. In particular, it finds itself at a velocity  $v_{sw}$  relative to the magnetic field which is convected outwards by the solar wind that is assumed to flow radially outwards. Due to the Lorentz force the PUI starts to gyrate about the magnetic field line on an orbit that is perpendicular to it. When we further consider a magnetic field's orientation that is perpendicular to the solar wind flow,  $\vec{B} \perp \vec{v}_{sw}$ , the ion's gyration speed is  $v_{sw}$  while its guiding center moves together with the field line at a speed of  $v_{sw}$  as well. Thus, the total speed of the PUI ranges between  $0 v_{sw}$  and  $2 v_{sw}$  in a sun frame of reference.

As the heliospheric magnetic field lines are shaped like an Archimedean spiral, the so called *Parker spiral*, the assumption of a perpendicular magnetic field only applies when solar wind speed  $v_{sw}$  and solar distance  $r_\odot$  follow the relation

$$90^\circ \approx \arctan\left(\frac{2\pi}{T_\odot \cdot v_{sw}} r_\odot\right)$$

with sun's sidereal period  $T_\odot \approx 25 \text{ d}$  (Prölss, 2004). In other cases, e.g. for solar distances about 1 AU, at which the angle between solar wind and magnet field direction

is approximately  $45^\circ$ , the maximum speed in a sun frame of reference is decreased. In general, the gyration speed is given by

*todo*

with ... .

The velocity space for a pickup situation with a non-radial magnetic field orientation is shown in figure *todo* on the right. The PUI's total velocity consists of the movement of the guiding center (...) and the gyration velocity (...). We note, that in this case there is a relative velocity between the motion of the solar wind bulk and the PUI's guiding center movement.

However, independent on the magnetic field orientation, every possible velocity space trajectory is part of a sphere with the radius  $v_{sw}$  centered around  $\vec{v}_{sw}$ . That means that, in the frame of the solar wind, the freshly created PUI always moves with a speed that is as fast as the solar wind itself. (*todo*: Hier w einführen?)

Instead of a single PUI we can consider an ensemble of PUI's that is injected into the solar wind while the magnetic field orientation is not changing much. For that we expect the VDF to form a ring shape in velocity space, commonly called the "PUI torus VDF" (Oka et al., 2002). The expected orientation of this highly anisotropic torus VDF depends on the local magnetic field direction and is sketched in figure *todo* for three different angles.

...thickness that is related (associated) to the neutral's velocity and is very small compared to the radius...

Spatial diffusion: chalov Fahr 1998. Signature of plasma parcel in which it was produced doesn't match with the one it is measured in

After the injection, the PUI population is radially carried away with the solar wind. During phase space transport through the heliosphere the PUIs are subjected to multiple processes that are expected to modify the shape of the initial toroidal VDF. However, it is not completely understood how the VDF evolves in detail.

A fast isotropization of the VDF due to pitch-angle scattering was suggested by Vasyliunas and Siscoe (1976) in a theoretical work. However, observations by e.g. Möbius et al. (1998) on *He+* or Gloeckler et al. (1995) on TODO have shown clear anisotropic features in the measured VDFs. Following studies (*todo*) explained these findings with the assumption that the ions would be injected into the sunward hemisphere of velocity space more likely. Ineffective pitch-angle scattering into the anti-sunward hemisphere thus would result in an radial anisotropy.

Recent observations have emphasized the influence of the magnetic field direction on the measured anisotropy. Utilising 2D analyses of the velocity space, Oka et al. (2002) and Drews et al. (2015) found that the measured VDF of PUIs is systematically oriented about the direction that is perpendicular to the magnetic field. Thus, it is believed that the VDF's anisotropic features are remnants of the initial toroidal VDF. (and the pa scattering didnt have enough time to isotropize the distribution)

Furthermore, there are different acceleration and deceleration processes that change

the PUI's initial VDF and lead to a diffusion in velocity space. Under the assumption of an isotropic VDF the PUI population is often treated as an adiabatic gas that is consequently cooled when expanding with the solar wind. This picture, initially suggested by Vasyliunas and Siscoe (1976), however, must be reviewed due to the doubtful fact of a fully isotropic VDF. Another cooling mechanism, called the *magnetic cooling*, is due to the magnetic field weakening with solar distance. As the PUIs are swept outwards both their ... and their ... invariant have to be conserved which leads to a decrease in both velocity components (parallel and perpendicular to the magnetic field) and thus to a decrease in total velocity (in the frame of the solar wind).

(focusing (adiabatic invariant) & Ginzberg Landau (Fahr2008): "magnetic cooling"  
(auch gute Erklärung: Fahr&Fichtner2011))

Acceleration of PUIs can be caused by acceleration: first and second order fermi (verstehen, Gründe): eher außen bzw. eher innen. Außerdem ein Mechanismus, der nicht an einzelne Events gebunden ist, sondern immer vorhanden: Mechanismus für alle Teilchen, power law -5...

man kann in der 1D Verteilung beobachten, dass  $2v_{\text{sw}}$  exceeded wird

PUI He should be measured throughout the mission as they penetrate the heliosphere until 0.5 AU (Gloeckler et al., 1992)

Instrument that is capable of measuring this distribution: large acceptance in absolute velocity, large variation and resolution in angles

### 1.5.1 1D reduced VDF, aim of this work...?

Warum sw frame?

Warum brauchen wir 3D? Um das zu entfalten und dann den Frame wechseln zu können.



## Chapter 2

# Instrumentation

### 2.1 Ulysses

The Ulysses spacecraft (Wenzel et al., 1992) was launched in 1990 and orbited the sun for nearly 20 years as a joint ESA/NASA project. Ulysses' most remarkable feature is its out-of-ecliptic orbit with a maximum heliographic latitude of  $80.1^\circ$ . As the first spacecraft it was hence capable of taking in situ measurements from above the poles of the sun.

The primary goal of the mission was to study the heliosphere in three dimensions. Some of the original main objectives were:

- to study the interplanetary magnetic field and the solar wind, especially its composition, the origin and waves and shocks within the solar wind plasma
- to investigate galactic cosmic rays and energetic particles
- to improve the knowledge about interplanetary dust
- to explore the neutral component of interstellar gas

Some secondary objectives included e.g. the investigation of Jupiter's magnetosphere during the Jupiter flyby and the search for gravitational waves and for gamma-ray burst sources (Wenzel et al., 1992).

For these aims Ulysses was equipped with a wide range of different instruments and antennas. One of the in situ instruments is the Solar Wind Ion Composition Spectrometer (SWICS), that will be described in the next section.

A sketch of Ulysses' unique orbit is shown in figure 2.1. Ulysses was launched in October 1990 and left earth's gravitational field with 15.4 km/s. Starting with a flyby manoeuvre around Jupiter Ulysses was sent onto its highly elliptical orbit. With an orbital period of 6.2 years Ulysses completed nearly three orbits around the sun until communication was shut down in June 2009 due to the expiring of the radioisotope thermal generators. Within the mission's long lifetime the Sun's behaviour over its activity cycle of 22 years could be studied.

Ulysses is a spin-stabilized spacecraft that spun at 5 rpm. The spin axis is aligned with the high-gain antenna's electrical axis, that provided a communication link from the spacecraft to Earth. The downlink bitrate was variable with up to 1024 bit/s during real-time connection.

TODO: Importance PUIs?

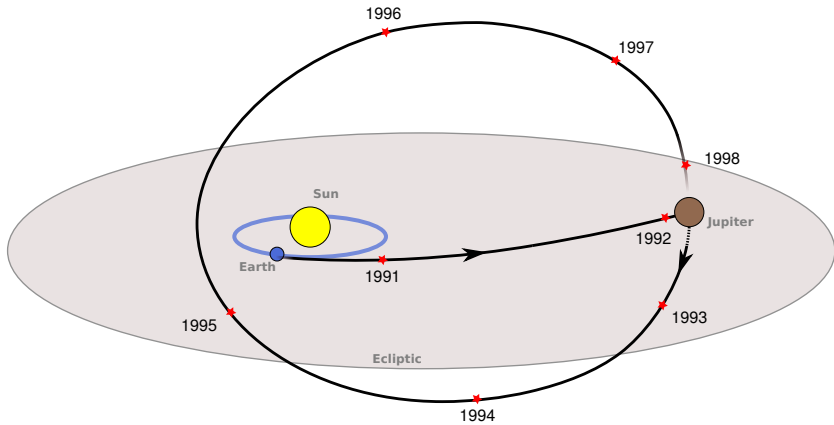


FIGURE 2.1: A sketch of Ulysses' first orbit. After the launch from earth in 1990 the spacecraft was sent to Jupiter from where it left the ecliptic on an elliptical orbit around the sun with perihelion at 1.3 AU and aphelion at 5.4 AU. Due to the orbit's high latitude of  $\sim 80^\circ$  Ulysses crossed the Sun's pole regions two times between 1994 and 1996. Figure after European Space Agency (2019).

## 2.2 SWICS

The Solar Wind Ion Composition Spectrometer (SWICS, Gloeckler et al. (1992)) is a time-of-flight mass spectrometer mounted on the spacecraft Ulysses (s. sec. 2.1). The instrument is designed to determine the elemental and charge-state composition and the velocity distribution of solar wind ions. With an energy-per-charge range from 0.16 kV to 59.6 kV SWICS is able to measure every solar wind ion species from protons to iron with any typical charge state. Depending on the individual ion, particle energies from 1 keV up to 1 MeV are covered.

SWICS is mounted on the sun-facing side of Ulysses and revolves around the spacecraft's spin axis with the spacecraft spinning. A photograph of the instrument is shown in fig. 2.2, left.

Ulysses SWICS also has a twin instrument that is the SWICS spare model, which has been mounted on the ACE spacecraft (Stone et al., 1998).

TODO: Super für measuring PUIs! viele wichtige Messungen...

SWICS measures the mass  $m$ , the charge  $q$  and the energy  $E$  of entering ions by a combination of three separate measurements: The electrostatic deflection analyzer within the entrance systems is used for determining the energy-per-charge of a particle. Within the time-of-flight/energy section the particle's time-of-flight and residual energy are measured. A more detailed description of the measurement is given in the next sections. A particle's trajectory through the instrument can be tracked in the schematic in fig. 2.3.

### 2.2.1 Collimator and Electrostatic Analyzer

Particles enter the instrument through the entrance collimator. It restricts particles to the ones with a trajectory that is parallel to the collimator slits. The collimator follows an intricate geometry that is fan-shaped with an opening angle of  $69^\circ$  in width and  $4^\circ$  in height and that is at the same time curved along its width. Fig. 2.2,



FIGURE 2.2:

*Left:* Photograph of the SWICS instrument. The fan-shaped collimator on top of the electrostatic deflection analyzer can be seen on the right. It is followed by the cylindrically shaped and silvery coloured *high-voltage bubble*, that contains the time-of-flight system, analog electronics and the sensor power supply. The gold-plated cylinder houses a  $-30\text{ kV}$  voltage supply. The opening angles of the collimator are  $69^\circ$  in width and  $4^\circ$  in height. OPT: Ausschneiden und beschriften

*Right:* Schematic cut through the sensor. In this view the orientation of the three solid state detectors is visualized. OPT: farbig markieren

Both figures are from from Gloeckler et al. (1992).

left, gives an idea of the shape.

After having entered through the collimator a particle has to pass the electrostatic analyzer. It is split up into two sections – energies-per-charge from  $0.16$  to  $14\text{ kV}$  are covered by the proton/helium channel. Particles within this range of energy will be filtered by their energy-per-charge and after an post-acceleration will be counted by a solid-state detector. As this simple measurement principle is very limiting for our analysis we will focus on the main channel that is suitable for a full *mass/mass-per-charge* analysis.

The main channel covers an energy-per-charge range of  $0.66$  to  $60.51\text{ kV}$ . A particle can only pass through the pair of curved deflection plates if its kinetic energy-per-charge equals a certain ratio that is given by the voltage between the two plates. To measure particles of different energy-per-charge the deflection voltage is stepped through 64 logarithmically spaced values, s. fig 2.4. As the voltage steps once per spin of Ulysses (every 12 s), a complete voltage cycle lasts  $\sim 12.8$  minutes. Every step has a relative uncertainty in energy-per-charge of  $\Delta\text{EpQ}/\text{EpQ} = 5\%$  that is due to the finite space between the plates.

### 2.2.2 Time-of-flight measurement

After having passed the electrostatic analyzer the ion is post-accelerated by an constant potential drop of  $30\text{ kV}$ . It enters the time-of-flight chamber with penetrating through a thin ( $\sim 3\text{ }\mu\text{g/cm}^2$ ) carbon foil from which secondary electrons are emitted. These electrons are guided to a microchannel plate detector where a start signal is triggered (s. fig 2.3). The stop signal is triggered after the ion has traversed nearly force free a distance of  $10\text{ cm}$  through the vacuumized time-of-flight section. Here it hits one of the solid-state detectors, where secondary electrons are emitted again. By

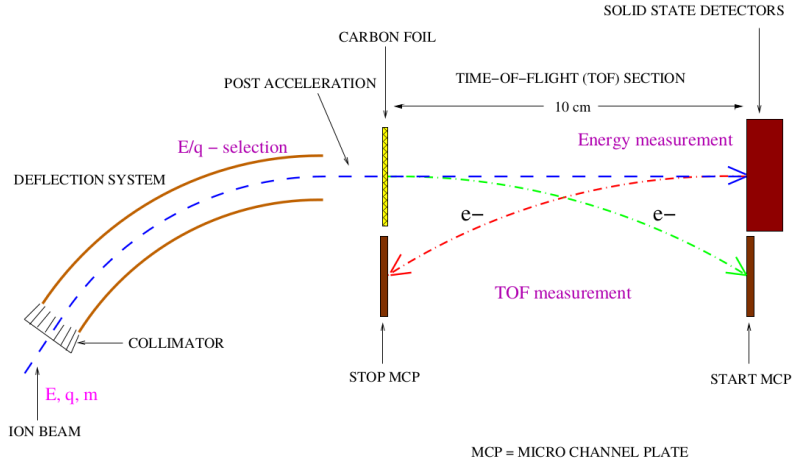


FIGURE 2.3: Schematic view of the SWICS detector. See text for reference. This figure is taken from Berger (2008).

combining the times of the start and the stop signal the particle's time-of-flight has been measured.

### 2.2.3 Energy measurement

Additionally, the ion's energy is measured when they hit one of the three solid state detectors.

A solid-state detector is realized by applying an inverse bias voltage to a semiconductor material. When ionized particles hit the material, they set free charge carriers from the resulting depletion zone. These charge carriers can be measured as a pulse of current which is proportional to the deposited energy of the ion.

Each of the three detectors has an active area of  $1.5 \times 1.3 \text{ cm}^2$ . Their alignment with each other can be seen in fig 2.2, right: While the central detector is oriented perpendicular to the symmetry axis of SWICS, the other two detectors are slightly tilted with respect to this axis. This way particles with different angles of incidence along the width of the collimator can be detected. The information on which of the three detectors has been hit will be utilized in chapter 3 for a coarse directional resolution of incident particles.

One of SWICS' main objectives is the measurement of the composition of incident particles. An ion and its charge state can be fully identified with the knowledge of its mass  $m$  and its mass-per-charge  $mpq$ . With the measurement of the time-of-flight  $ToF$ , the energy  $E_{SSD}$  and the knowledge of the energy-per-charge  $EpQ$  we can calculate the mass  $m$ , the mass-per-charge  $mpq$  and velocity  $v$  of an ion  $i$  with the following set of equations:

$$m_i = 2 E_{SSD} \left( \frac{Tof}{d} \right)^2 \quad (2.1)$$

$$mpq_i = 2 (EpQ + V_{PAC}) \cdot \left( \frac{Tof}{d} \right)^2 \quad (2.2)$$

$$v_i = \sqrt{2 EpQ \frac{1}{mpq_i}} \quad (2.3)$$

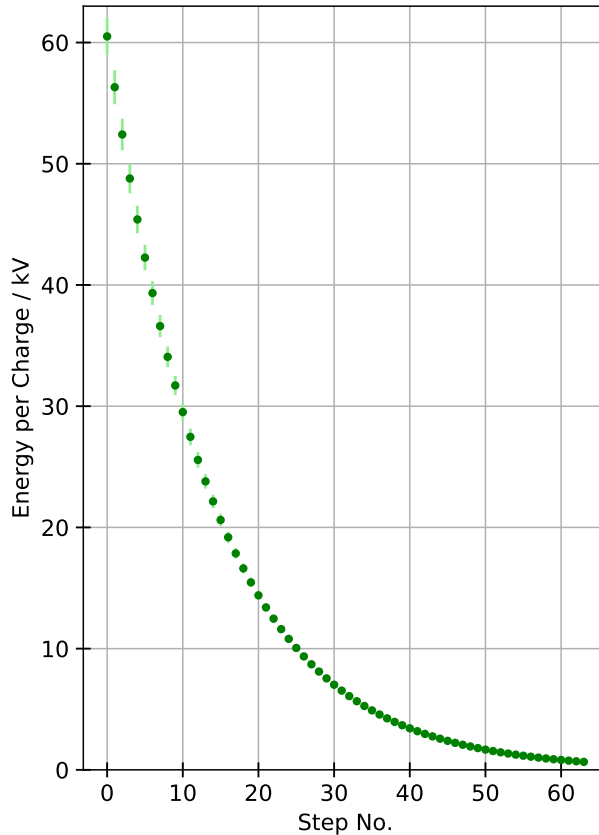


FIGURE 2.4: Energy-per-Charge steps of Ulysses SWICS. A voltage cycle starts with step 0 that is the highest voltage  $E_pQ = 60.51$  kV. Voltage is then swept down 64 logarithmically spaced steps up to  $E_pQ = 0.66$  kV. The uncertainty of the single steps is  $\frac{\Delta E_pQ}{E_pQ} = 5\%$  and drawn in lighter color.

where  $d$  is the length of the time-of-flight section and  $V_{PAC}$  is the post-acceleration voltage.  $v$  denotes the ion's initial velocity when entering the instrument and is not to be confused with its velocity during the time-of-flight measurement, that is altered particularly by the post-acceleration.

## 2.3 Data products

Direct Pulse-Height Analysis data (PHA data) are one of SWICS' data products and the ones that are most relevant for the analysis in this work.

Over one voltage cycle SWICS steps through the 64 energy-per-charge steps of the electrostatic analyzer (s. sec 2.2.1), which we call ESA steps. At normal spacecraft telemetry rates SWICS steps once per spin, which is once every 12 s. During these times 30 PHA words per spin are selected and transmitted. The selection is based on a priority scheme that is described below in sec. 2.3.2.

Every 24-bit PHA word contains following information on an incident particle that triggered a valid measurement:

- $E_{SSD}$ : Energy deposition in the solid state detector measured through 256 channels in a range 40 – 600 keV

- *ToF*: Time-of-Flight  
measured through 1024 channels in a range 10 – 200 ns
- Sector information:  
SWICS divides one spin of Ulysses up into 8 sectors of approximately equal duration. This yields information on the spatial origin of particles.
- Detector information:  
Which of the three solid state detector elements has been triggered?
- Priority category:  
Due to limited telemetry only an assorted sample of all measured particles can be transmitted. This selection is based on different priorities. For details see [2.3.2](#).

The interpretation of a set of PHA words that have been collected over time is discussed in sec. [2.4](#).

### 2.3.1 Detection Efficiency

When working with SWICS – like for any physical measurement – one has to consider several constraints that impede the ideal measurement as it is described in sec. [2.2](#).

One of these constraints is the detector efficiency, which describes the probability to measure a particle that has entered the instrument (Todo: ?). With an ion passing through the time-of-flight section there is the likelihood that secondary electrons may not be emitted properly from the carbon foil and solid state detector which then leads to an invalid time-of-flight measurement. Also, ions could pass through the time-of-flight section on divergent trajectories due to scattering processes (TODO: in the carbon foil??). Subsequently, the ion possibly does not hit the sensitive area of the solid state detector and would neither trigger a stop signal for the time-of-flight measurement nor a valid energy measurement in the solid-state detector.

Another reason for an invalid energy measurement in the solid-state detector can be that the ion's energy is smaller than the threshold of the solid-state detector. In this case, only energy-per-charge and time-of-flight information for the ion are available. Such events without a corresponding energy measurement are called double coincidences, while events with triggered start and stop signal and an energy measurement are called triple coincidences.

The reason for choosing a non-zero threshold is to limit the influence of the solid-state detector's natural noise. For SWICS this noise level is quite high, at around 12 keV (Gloeckler et al., [1992](#)) (todo: ?), so that the threshold is chosen to be  $\sim 30$  keV. The detection efficiency is highly dependent on the ion species and deflection step. Ions with a small mass and charge are most likely to not overcome the threshold at low energy-per-charge values. For the bulk of  $\text{He}^+$  this is already the case for ESA step 17 ( $E_p Q = 17.86$  kV), which corresponds to a  $\text{He}^+$  velocity of  $v = 900 \text{ km s}^{-1}$  (s. eq. [2.3](#)).

Unfortunately,  $\text{He}^+$  detection efficiencies are not known to us for Ulysses SWICS. Instead, we make use of the efficiencies from ACE SWICS, that have been calculated by Kötén ([2009](#)). As ACE SWICS uses different energy-per-charge ranges we had to extrapolate the values for Ulysses SWICS. For the highest energy-per-charge value  $E_p Q = 60.51$  keV we interpolated the efficiency from the ACE  $\text{He}^+$  triple efficiencies and then extrapolated linearly to an efficiency of 0 at ESA step 17. By this, we accommodate for the above mentioned fact that  $\text{He}^+$  does not have enough energy

to deposit energy above the solid state detector's threshold at ESA step 17 and thus, the probability for a triple coincidence is zero.  $\text{He}^+$  efficiencies from ACE SWICS and the resulting efficiencies used for Ulysses SWICS are shown in fig. 2.5. For sure, these values are not realistic but represent the overall trend of a decreasing efficiency for higher ESA steps.

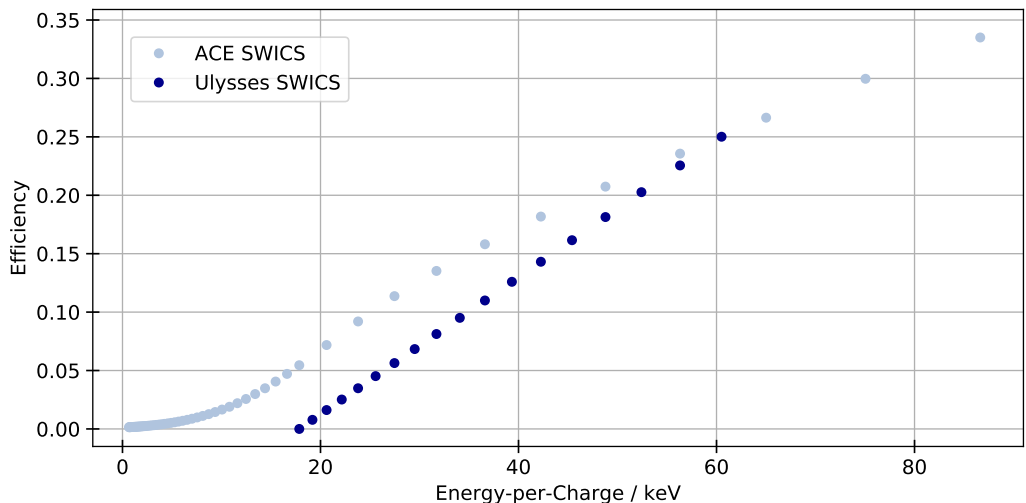


FIGURE 2.5:  $\text{He}^+$  detection efficiencies for ACE SWICS over all ESA steps from 0.66 kV to 86.64 kV. For Ulysses SWICS the efficiencies have been extrapolated between 0 for ESA step 17 ( $E_{pQ} = 17.86 \text{ kV}$ ) and the highest efficiency for ESA step 0 ( $E_{pQ} = 60.51 \text{ kV}$ ). The latter value has been interpolated from the ACE efficiencies.

### 2.3.2 Priority Weighting

SWICS' data processing unit performs an on-board mass and mass-per-charge-classification. For every ion with valid measurements the mass  $m$  and mass-per-charge  $mpq$  are calculated based on the measurements of  $E_{\text{SSD}}$ ,  $ToF$  and the particle's ESA step using a look-up-table technique.

On the one hand these values are used for sorting the ions into predefined boxes in the  $m$ - $mpq$ -space which yield in the so-called matrix rate, a second data product that is provided beneath the PHA words.

Secondly, and more important for our analysis, the  $m$  and  $mpq$  information is used to sort every measured ion into one of three priority ranges. Due to a limited telemetry possibly not every measured particle can be transmitted as a PHA word. 30 PHA words per spin are chosen from these ranges in way that the ratio of low and high priority PHA words is balanced. By this selection less abundant heavier ions are artificially enhanced which is necessary to recreate the measured composition from the transmitted PHA words. Table 2.1 shows a summary of this priority scheme. Details about this can be found in Gloeckler et al. (1992).

To account for the priority biased selection of PHA words it is necessary to weight the transmitted data with the so-called base-rate weight  $brw = \frac{D_{\text{PHA}}}{T_{\text{PHA}}}$ , where  $T_{\text{PHA}}$  is the number transmitted PHA words and  $D_{\text{PHA}}$  the number of detected particles on which this PHA word is based. The measured composition can be restored in this way.

TABLE 2.1: SWICS' priority categorization scheme

Range 0	$m < 8.7$ ; $m_0 : mpq < 3.3$	H, He <sup>+</sup> , He <sup>2+</sup> ; Doubles
Range 1	$m > 8.7$	Heavier ions
Range 2	$m_0 : mpq > 3.3$	Doubles

## 2.4 ET matrices, identification

Fig. 2.6 shows longterm PHA data collected over two years with Ulysses SWICS for ESA step 24 ( $EpQ = 10.8$  kV). For every particle with valid time-of-flight and energy measurements the  $E_{SSD}$  channel is plotted over the time-of-flight channel. As a particle's mass and mass-per-charge are connected to the measured values  $EpQ$ ,  $ToF$  and  $E_{SSD}$  by equations 2.1 – 2.3, every ion species occupies a distinct position in this histogram, which we call ET-matrix. However, due to uncertainties in the measurements of  $EpQ$ ,  $ToF$  and  $E_{SSD}$  an event may be displaced around its ideal position. For multiple events of the same species this results in broadened distributions. A detailed discussion on these uncertainties can be found for example in Berger (2008). We can identify several ion species in the shown ET-matrix: A selection of those is labelled in 2.6.

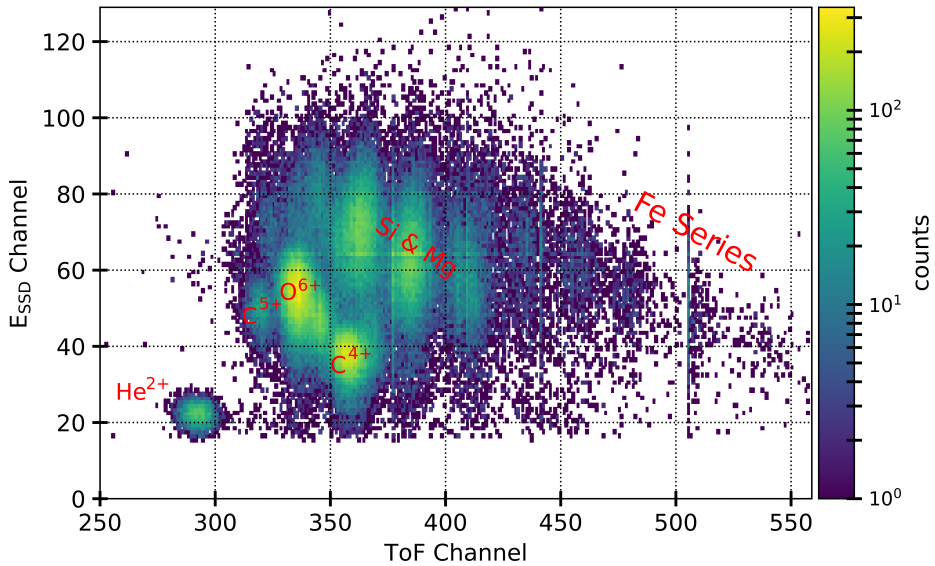


FIGURE 2.6: ET-matrix from Ulysses SWICS PHA data of years 1993–1994. All plotted events were measured during ESA step 24 ( $EpQ = 10.8$  kV). Only triple coincidences are shown. Besides accumulated counts in ion-specific positions, there are a few horizontal and vertical stripes apparent in the shown ET-matrix – for example in  $E_{SSD}$  channel 65 and time-of-flight channel 409, 377 or 505. These are imprints of irregularities within SWICS' Analog-Digital-Converters which can be noticed as a saturation of one bin while the adjacent bin is depleted. However, these signatures are not expected to have a significant effect on the following analysis.

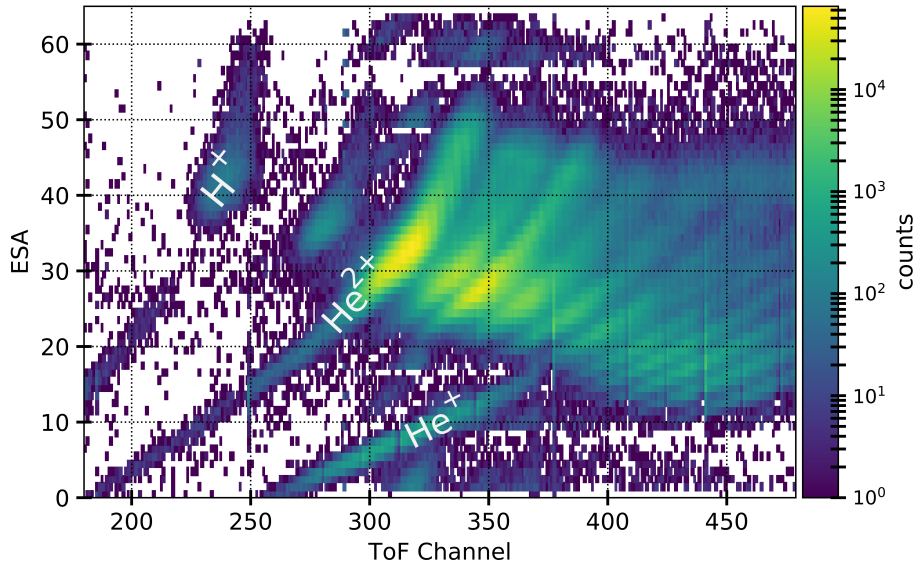


FIGURE 2.7: Histogram over time-of-flight and ESA channels of two years (1993-1994) of Ulysses SWICS Triple Coincidence PHA data. Note, that the ESA channel numbers are inversely proportional to the energy-per-charge values. Ion species with the same mass-per-charge ratio can be detected on curves  $ESA \sim ToF^2$ .

#### 2.4.1 Selection of $\text{He}^+$

For extracting only the  $\text{He}^+$  events from the PHA data we histogram the events' energy-per-charge against their measured time-of-flight in fig. 2.7. Ions with the same mass-per-charge can be tracked on curves with  $ESA \sim ToF^2$ , while species with higher masses-per-charge can be found on curves at higher  $ToF$  channels. This way one can identify for example  $\text{H}^+$  and  $\text{He}^{2+}$ .

At the bottom of fig. 2.7 suprathermal  $\text{He}^+$  clearly stands out. For time-of-flight channels above  $\sim 375$  heavier solar wind ions with similar mass-per-charge ratios (e.g.  $\text{Si}^{7+}$ ) mix into the  $\text{He}^+$  population. We can take advantage of SWICS' on-board priority weighting, that has been described in sec. 2.3.2. By selecting Triple Coincidences with Range-0 priority only we separate out events with  $m > 8.7 \text{ u}$ . This leaves us mainly with  $\text{H}^+$ ,  $\text{He}^{2+}$  and  $\text{He}^+$  as the prominent ions in the Range-0 mass range. The result is shown in fig. 2.8. One can also see traces of heavier ions seeping into the Range-0 regime but this does not affect those ESA steps in which  $\text{He}^+$  is present. For a final selection we define a box around the  $\text{He}^+$  population and extract all events within this box. The result is shown in fig. 2.9, above.

As explained in sec. 2.3.1, with  $\text{He}^+$  we are limited to ESA steps 0 to 19 when only considering Triple Coincidences. For higher ESA steps  $\text{He}^+$  only occurs as a double coincidence. Double coincidences are not sufficient for us, as we need the information about which solid-state detector has been triggered for a directional analysis.

The presented selection procedure has been performed on the complete data set from 1991 to 2009 resulting in a total of  $\sim 1.6 \cdot 10^5$   $\text{He}^+$  PHA words and an average of  $\sim 8.5 \cdot 10^3$   $\text{He}^+$  PHA events per year. This corresponds in average to one measured  $\text{He}^+$  event every five voltage cycles. Note, that there is a wide variation between different periods of time. PHA numbers per year are listed in fig. 3.12.

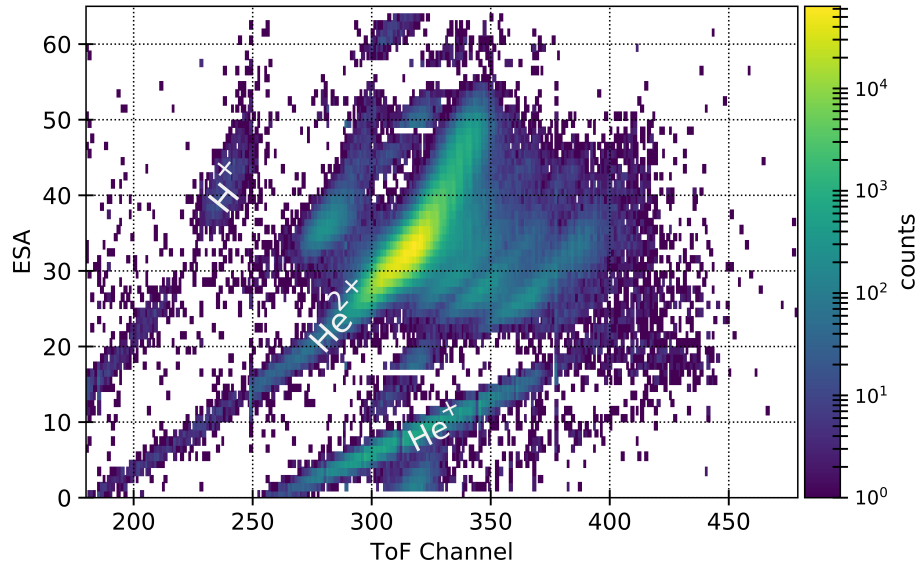


FIGURE 2.8: The same histogram as in fig. 2.7, but this time only events with Range-0 priority are plotted. This basically removes ions with  $m > 8.7 \text{ u}$ .

#### 2.4.2 Selection of $\text{He}^{2+}$

For testing the virtual detector in chapter 3 we need a species of which we know that it mainly moves with the solar wind bulk and that occurs within the Triple Coincidences, so that we have directional information. We choose for  $\text{He}^{2+}$ , the most abundant ion in the solar wind (Prölss, 2004, ch. 6.1) as it also occurs in Range 0 and is easily recognizable in fig. 2.8. Unlike  $\text{He}^+$ ,  $\text{He}^{2+}$  can also be found at ESA steps higher than step 19, as it gains more energy when being post-accelerated due to the twice as high charge. Thus,  $\text{He}^{2+}$  deposits more likely energies above the threshold of the solid-state detector. We selected  $\text{He}^{2+}$  with the same procedure as for  $\text{He}^+$ . However, in this case it is not so crucial to include exactly every  $\text{He}^{2+}$  event, as we do not want to perform a full analysis with  $\text{He}^{2+}$ . The resulting selection is shown in 2.9, below.

TODO: woher sind überhaupt die PHA Daten?

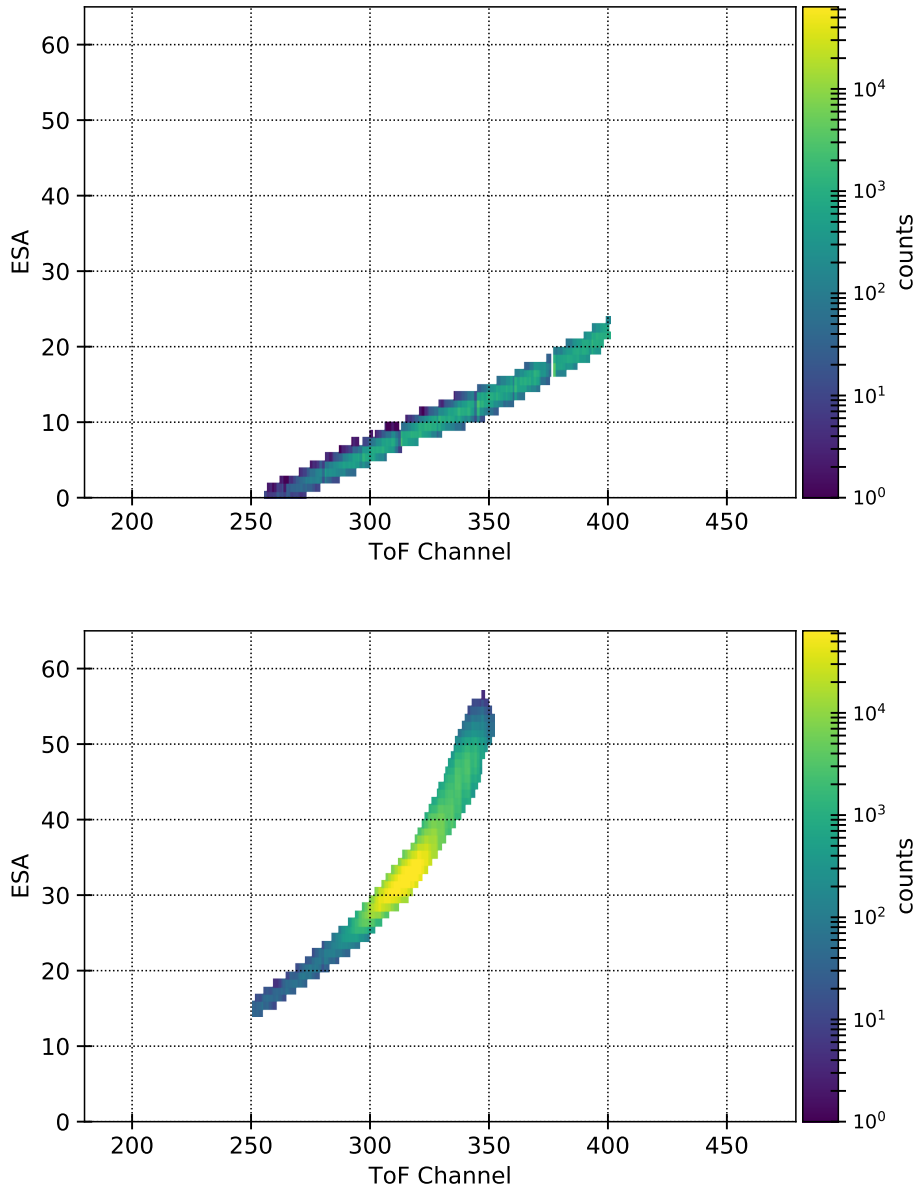


FIGURE 2.9:  $\text{He}^+$  (above) and  $\text{He}^{2+}$  (below) selections that have been cut out from fig. 2.8.



## Chapter 3

# Data Analysis and Methods

In this chapter we combine the prepared SWICS data from chapter 2 with position and orientation information of the Ulysses spacecraft with help of a model of the SWICS detector.

### **Todo:**

(This way we can take the step from the directional incident information of a measured ion to its position in velocity space.)

(...)

In a first step the two main coordinate systems of this work are introduced.

## 3.1 Coordinate Systems

In the following analysis the SWICS PHA data will be connected to the position and orientation of the Ulysses spacecraft. For this two different coordinate systems are utilized.

### 3.1.1 Heliographic Coordinate System

Trajectory data from Ulysses Final Archive (2008) is used in this work to describe Ulysses' orbit. In this data, Ulysses' position is given in daily intervals and based on different coordinate systems, including the heliographic coordinate system in the B1950.0 epoch.

The heliographic (HG) coordinate system is a Cartesian Sun-centered system with the Sun's equatorial plane as a reference plane. Its X-axis is directed along the line of ascending node, which is the intersection line of the ecliptic and the solar equatorial plane. While the latter has an inclination of  $i_{\odot} = 7.25^\circ$  against the ecliptic (Fränz and Harper, 2002) the line of ascending node is at an ecliptic longitude of  $\Omega_{\odot} \approx 75^\circ$  relative to the First Point of Aries in 1950 (NASA HelioWeb, 2019). The Z-axis of the HG coordinate system is directed along the Sun's spin axis (northward) and the Y-axis completes the right-handed system.

In HG spherical coordinates the longitude  $\varphi_{\text{HG}}$  is defined to be  $0^\circ$  for directions along the X-axis and increases towards the Y-axis. The latitude  $\vartheta_{\text{HG}}$  is  $0^\circ$  for directions within the solar equatorial plane and  $+90^\circ$  for northward directions.

However, when working with the Ulysses trajectory data it was found that these data were given in spherical coordinates for which  $\varphi_{\text{HG}} = 0^\circ$  was towards  $-105^\circ$  ecliptic longitude relative to the First Point of Aries. This means that the Ulysses trajectory coordinate system is shifted  $180^\circ$  around the solar spin axis against the classical definition (s.a.).

In fig. 3.1 Ulysses' spherical HG coordinates as well its distance from the Sun are given over time of the mission.

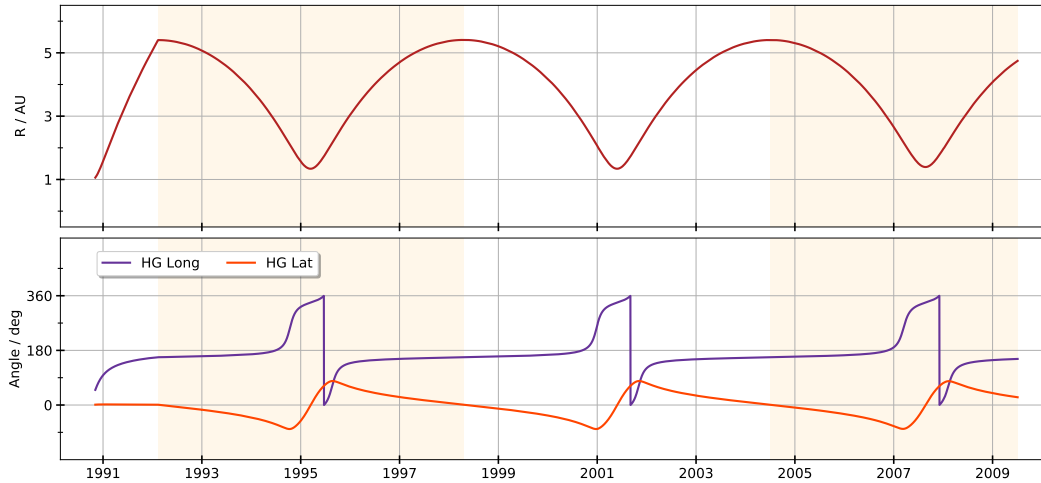


FIGURE 3.1: Ulysses trajectory data from November 1990 to June 2009 based on the data from the Ulysses Final Archive (2008). Color shaded are the three orbits of the mission. **Above:** Shown is Ulysses' radial distance  $R$  from the Sun. Perihelion and aphelion of the space-crafts' elliptical orbit can clearly be seen as the nearest/farthest distance that is 1.3 AU and 5.4 AU. Over the duration of the mission Ulysses passes each of these points every 6.2 years and three times in total. **Below:** Shown are Ulysses' HG longitude and latitude. Note, that the longitude is shifted around  $180^\circ$  with respect to the classical definition (s. text for details). A clear periodicity over Ulysses' three orbits can be seen. Maximum and minimum latitude are  $\sim \pm 80^\circ$ . These points are highest above the poles of the Sun and are reached a few weeks before and after Ulysses' pass through the perihelion.

**TODO: Fontsize größer**

### 3.1.2 Radial Tangential Normal Coordinate System

Ulysses' orbit has been described in the HG coordinate system, which is a coordinate system that is fixed with respect to the Sun. For describing positions and velocities in the frame of the spacecraft (e.g. the Aspect Angle) we need a coordinate system that moves with the spacecraft.

When dealing with Ulysses' trajectory data it is useful to work with Radial Tangential Normal (RTN) coordinates. The RTN coordinate system is defined relative to a moving object in the heliosphere, in this case Ulysses, and is centered at the Sun. A graphical representation of the system is given in fig. 3.2. The unit vectors are  $\vec{R}$ ,  $\vec{T}$  and  $\vec{N}$ , where  $\vec{R}$  points radially outward from the Sun to the current position of the spacecraft.  $\vec{T}$  is defined as the normalized cross product of the Sun's angular velocity,  $\vec{\omega}$ , and  $\vec{R}$ .  $\vec{N}$  completes the right-handed Cartesian coordinate system. Consequently, the RTN system is not defined for a spacecraft's position right above one of the Sun's poles as the cross product  $\vec{\omega} \times \vec{R}$  is zero here. Nevertheless we do not have to worry about this fact as Ulysses did not cross the poles directly.

OPT: Umrechnung von HG in RTN?

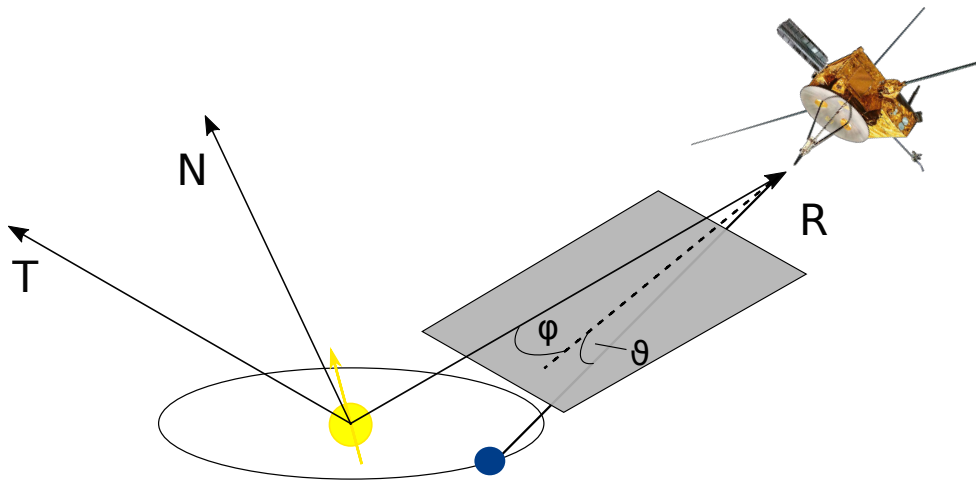


FIGURE 3.2: Graphical representation of the RTN coordinate system (not to scale). Shown are the Sun (yellow) and the Earth (blue) and the Ulysses spacecraft at a non-specific position on its orbit.  $\vec{R}$  is defined as the unit vector along the Sun–Earth line,  $\vec{T}$  as the normalized cross product  $\vec{\omega} \times \vec{R}$  with  $\vec{\omega}$  the angular velocity of the Sun (yellow vector).  $\vec{N}$  completes the right-handed Cartesian system. Also shown is the definition of the aspect angle components  $\varphi_{\text{asp}}$  and  $\vartheta_{\text{asp}}$  as they are used in this work. The grey plane depicts the  $\vec{R}-\vec{T}$  plane.  $0^\circ < \varphi_{\text{asp}} < 90^\circ$  and  $-90^\circ < \vartheta_{\text{asp}} < 0^\circ$  in the shown situation. **TODO: Zeichnung anpassen: Vektorpfeile, Indizes Winkel; Quelle Ulysses Dingsi**

## 3.2 The Detector Model

**Intro TODO:**

With SWICS' measurement of detector and sensor (todo: Verweis Kapitel, vielleicht explizit schreiben...?) we can obtain directional information about the velocity of incident ions. However, a sec-det information alone is not sufficient to determine the ion's three dimensional velocity. Its meaning is highly dependent on SWICS' orientation and the eigen-velocity of the spacecraft. Additionally, SWICS' collimator is characterized by an intricate geometry, making an analytical solution of the problem difficult.

Instead, we choose to use a virtual detector as a numerical approach. The initial idea of modelling the SWICS detector comes from Dr. Lars Berger who constructed a similar model for ACE SWICS. This work focusses on establishing the model for Ulysses SWICS.

Kurze Zusammenfassung, was der virt. D. macht?

### 3.2.1 Construction

For reconstructing the velocity space that is observed by SWICS we need to know about the directions of incident particles that can enter the instrument. These directions are limited by the instrument's entrance system.

The original geometry of the SWICS entrance system, in particular the collimator,

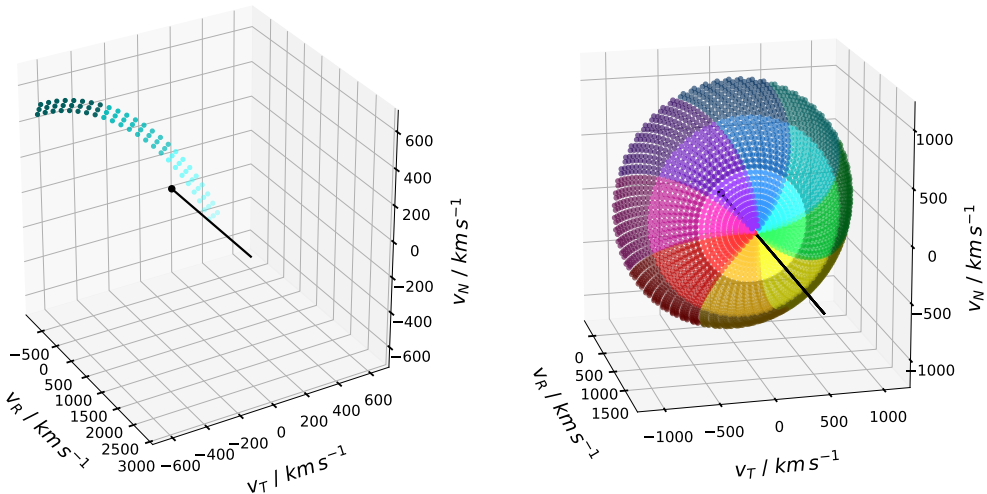


FIGURE 3.3: Todo:

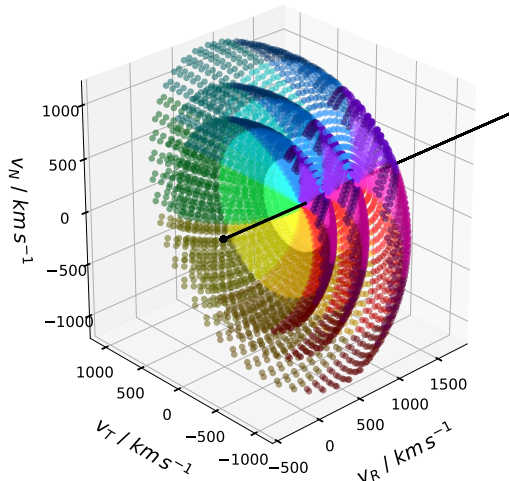


FIGURE 3.4: TODO

was read out from a technical drawing. To illustrate the intricate geometry, a photo of a 3D printed model of the entrance system is shown in fig. 3.5.

The instrument is mounted with one of the collimator's narrow side edges parallel to Ulysses' spin axis. When we define this edge to be lying on the x-axis of a three dimensional Cartesian coordinate system, the collimator geometry can be reconstructed by revolving this edge for  $90^\circ$  around a straight line that lies in the xy-plane with an angle of  $56^\circ$  relative to the x-axis. Every third of these  $90^\circ$  is reserved as the opening angle for each of the three detector elements that are described in sec. 2.2.

The detector's field of view is the solid angle over which the detector is sensitive to incoming particles. It can be represented by a set of outward directed normal vectors on the opening plane of the detector. In our model, we have a variable number  $n_d$  of these equidistant vectors which we can divide along the width and the height of the detector opening. The real continuous field of view is modelled better with an



FIGURE 3.5: FOTO SWICS 3D

3D printed model of SWICS' entrance system, that was made from original CAD files. Its geometry can be described by a cut of 90 deg longitude (**todo: latitude? 4 grad?**) from a sphere (of **r ca. 26 cm ?**) at  $todo^\circ$  polar latitude. The resulting piece is not flat but curved and has a height of  $\sim 5$  cm. This geometry leads to two deflection plates that are curved but have a constant distance of  $\sim 3.7$  cm over a relatively large area which is necessary to provide a constant voltage for the energy-per-charge filtering action (s. 2.2.1). The resulting opening angles of the collimator are  $69^\circ$  in width and  $4^\circ$  in height.

increasing number of normal vectors that cover the opening.

Each of these normalized vectors  $\mathbf{f}_i$  has a unique direction  $\mathbf{f}_i = [f_{x,i} \ f_{y,i} \ f_{z,i}]'$  in position space.

With a spin of the Ulysses spacecraft the fixedly mounted SWICS instrument is revolved around the spacecraft spin axis. One revolution of SWICS is divided up into eight sectors of approximately equal duration respectively of  $45^\circ$  each (s. sec. 2.3). As the spacecraft is spinning continuously, also the field of view changes its rotation angle continuously. For our virtual detector we model this by rotating the field of view gradually over  $n_{sec}$  steps through every sector.

The integrated field of view over one spin then comprises  $n_{FoV} = n_d \cdot n_{sec} \cdot 8$  single vectors  $\mathbf{f}_i$  which are directed symmetrically around the spin axis. An example is shown in fig. 3.3, right, for  $n = bla\dots$ .

### From Field of View to Velocity Space

The detector's velocity acceptance can be calculated by combining the directional information from the field of view with the value of absolute velocity from the current ESA step.

A particle can only enter the detector when its absolute velocity is within the acceptance of the current EpQ step and when its inverted direction is within the detectors field of view. For a given acceptance velocity  $v_i$ , each field of view vector  $\mathbf{f}_i = [f_{x,i} \ f_{y,i} \ f_{z,i}]'$  can be associated with an acceptance velocity vector

$$\mathbf{v}_i = \begin{bmatrix} v_{R,i} \\ v_{T,i} \\ v_{N,i} \end{bmatrix} = - \begin{bmatrix} f_{x,i} \\ f_{y,i} \\ f_{z,i} \end{bmatrix} \cdot v_i. \quad (3.1)$$

The resulting acceptance of the fixed instrument for  $n = todo$  and  $v = todo$  is shown in fig. 3.3, left.

With consideration of the integrated field of view over one spacecraft spin the acceptance velocity for a distinct velocity  $v_i$  consists of the combination of  $n_{\text{FoV}}$  discrete velocities (TODO: Schmissigeres Wort suchen. Velocity-Akzeptanzpunkte...?) which form a shell with radius  $v_i$  in velocity space, s. fig. 3.3, right, for  $v_{\text{todo}}$ )

The central velocity for an ion of charge  $q$  and mass  $m$  at an ESA step with energy-per-charge  $EpQ$  (in keV/e) is

$$\frac{v_c}{\text{km s}^{-1}} = \sqrt{\frac{2 \cdot EpQ \cdot 1.602 \cdot 10^{-19} \cdot |q|}{m \cdot 1.661 \cdot 10^{-27}}}$$

with  $m = 4 \text{ u}$  and  $|q| = 1 \text{ e}$  for He<sup>+</sup>.

Different absolute velocities  $v$  appear as distinct shells of radius  $v$  in velocity space. To get an idea of this, an example with three of those (todo: v bzw ESA angeben) shells is shown in fig. 3.4. (TODO: Ich brauche auch noch ein Bild mit einzelner Schale ohne AA-Auslenkung, so wie das FoV-Bild (s.u., Vergleich im AA Kapitel)) To represent the uncertainty in the energy-per-charge measurement, we take into account the relative uncertainty  $\Delta \frac{E}{q} / \frac{E}{q} = \pm 2.5\%$  (Gloeckler et al., 1992) and translate it into an uncertainty  $\Delta v/v = \frac{1}{2} (\Delta \frac{E}{q} / \frac{E}{q}) = \pm 1.25\%$  in accepted velocity. For every ESA step we can now choose a number of  $n_{epq}$  single velocities that are distributed evenly in the interval  $[v_c - \Delta v/v, v_c + \Delta v/v]$ .

With combining all  $64 \cdot n_{epq}$  shells we obtain a dense three dimensional pattern of accepted velocities that simulate the real continuous velocity acceptance volume of the spinning detector.

When we measure a PHA word with a distinct sector, detector and ESA information, we can now determine its three dimensional velocity with our virtual detector. Of course, the resolution is limited as sector and detector areas are finite as well as the uncertainty  $\Delta \frac{E}{q} / \frac{E}{q}$ . By spreading the count over the entirety of  $n_{epq}$  velocity acceptances (Todo: besseres Wort, s.o.) in the volume of the sector- detector-ESA combination, we take into account every velocity that could have led to this distinct PHA word.

Todo: Später schreiben, was für n verwendet wurden

### 3.2.2 Ulysses' Eigen-velocity

For the considerations in the previous section we assumed a detector on a spacecraft that is fixed in space. Obviously this is not the case for the Ulysses spacecraft, which moves on its elliptical orbit around the Sun.

For determining the spacecraft's velocity we make use of the daily trajectory data from sec. 3.1. For every point in time  $t_i$  we calculate the spacecraft's instantaneous velocity  $v_{SC,i}$  by forming the differential quotient

$$v_{SC,i} = \frac{\begin{bmatrix} R_{i+1} \\ T_{i+1} \\ N_{i+1} \end{bmatrix}_i - \begin{bmatrix} R_i \\ T_i \\ N_i \end{bmatrix}_i}{t_{i+1} - t_i}$$

with  $t_{i+1}$  being the time of the next trajectory data given, which is normally  $t_i + 1 \text{ d}$ . Note, that the spacecraft's position at  $t_{i+1}$  has to be considered in the RTN coordinate

system that relates to the spacecraft's position at  $t_i$ . The resulting velocities in RTN coordinates are shown in fig. 3.6 and range between  $-20 \text{ km s}^{-1}$  and  $35 \text{ km s}^{-1}$ .

To correct the measured velocities for the spacecraft's eigen-velocity, we add the resulting velocity components to the velocity acceptance. Thus, for every instant in time the shells in fig. 3.4 are shifted a bit in velocity space based on the respective eigen-velocity.

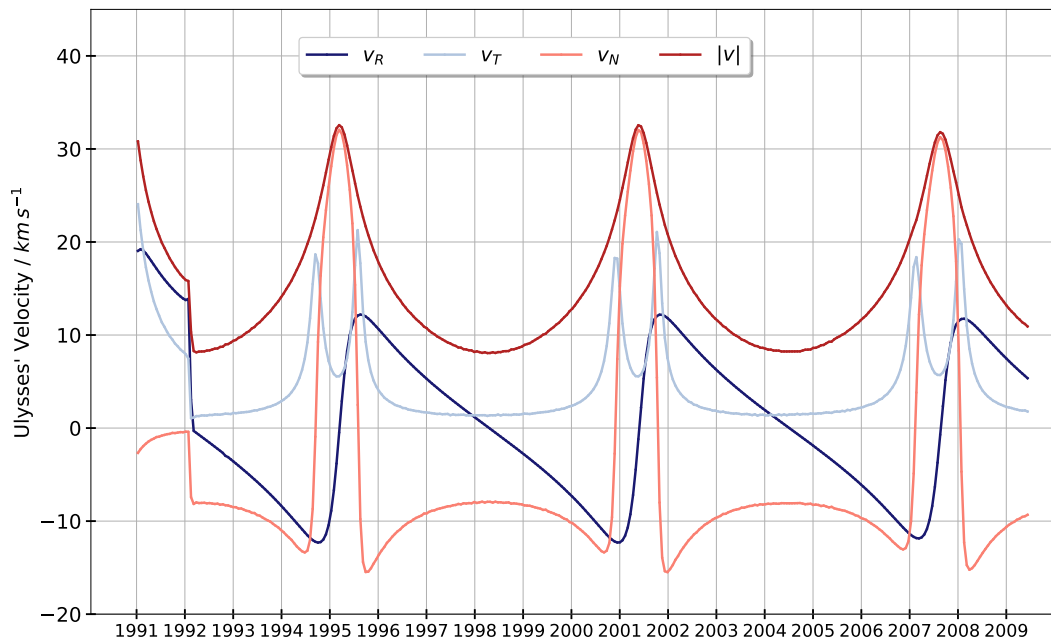


FIGURE 3.6: Plot Eigengeschwindigkeit

### 3.2.3 Orientation of the Detector

Until now we have assumed that Ulysses' spin axis is aligned with the R-axis of the coordinate system, i.e. that the spin axis points directly to the Sun. In fact, this is not the case in general. Due to telemetry reasons, Ulysses' high gain antenna has to be oriented directly towards Earth. As Ulysses' spin axis is aligned with the electrical axis of the antenna (Wenzel et al., 1992), it has an offset towards the spacecraft-Sun line. This offset is called aspect angle and is a permanently changing quantity as a function of Ulysses' position and the position of the Earth. Because a varying aspect angle results in SWICS covering different parts of velocity space it is essential to consider this quantity in detail.

#### Calculation of the Aspect Angle

The aspect angle is measured from the Ulysses–Sun line to the Ulysses–Earth line. To describe this angle uniquely for any moment, we need two spherical coordinates  $\varphi_{\text{asp}}$  and  $\theta_{\text{asp}}$  based on the RTN system. As shown in fig. 3.2,  $\varphi_{\text{asp}}$  is measured in the  $\vec{R}-\vec{T}$  plane between  $-\vec{R}$  and the projection of the Ulysses–Earth line into this plane.  $\varphi_{\text{asp}}$  is  $0^\circ$  for directions along  $-\vec{R}$ , that is the Ulysses–Sun, and increases to positive values towards  $-\vec{T}$ .  $\theta_{\text{asp}}$  is the angle between the projection of the Ulysses–Earth

line into the  $\vec{R}-\vec{T}$  plane and the line-of-sight(TODO) itself. It is defined as  $0^\circ$  for directions that lie within the  $\vec{R}-\vec{T}$  plane and  $+90^\circ$  for directions along  $\vec{N}$ .

For the calculation of the aspect angle we use the Ulysses trajectory data (s. sec. 3.1) and Earth trajectory data in heliographic coordinates on a daily basis from NASA HelioWeb (2019) and converted both to RTN coordinates. In fig. 3.7 both components  $\varphi_{asp}$  and  $\vartheta_{asp}$  as well as the “flat” aspect angle  $\alpha$  with  $\alpha = \arccos(\cos \varphi_{asp}) + \arccos(\cos \vartheta_{asp}) - 1$  are shown over the time of the mission.  $\varphi_{asp}$  varies in the range from  $\sim -25^\circ$  to  $\sim 42^\circ$  and  $\vartheta_{asp}$  in a range from  $\sim -30^\circ$  to  $\sim 17^\circ$ . Large angles occur especially around the three fast latitude scans, i.e. when Ulysses is at its perihelion and has the smallest distance to Sun and Earth.

(Todo: Lars fragen, ob die genaue Rechnung hier rein soll, Kladde S. 79)

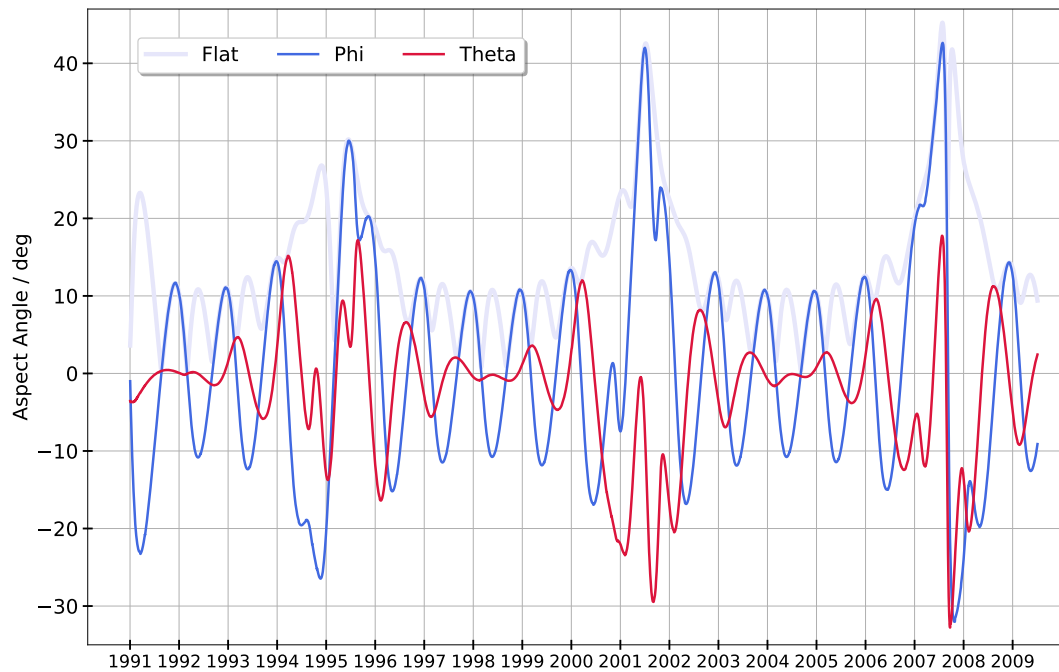


FIGURE 3.7: The evolution of Ulysses’ aspect angle components  $\varphi_{asp}$  and  $\vartheta_{asp}$  and the “flat” aspect angle  $\alpha$  with  $\alpha = \arccos(\cos \varphi_{asp}) + \arccos(\cos \vartheta_{asp}) - 1$  from 1991 to the end of the mission. The aspect angle is the angle between the Ulysses-Sun line and the orientation of Ulysses’ spin axis. A constantly changing aspect angle results from the fact that the spacecraft’s antenna, that is nearly parallel with the spin-axis, has to point towards Earth all the time. Particularly large aspect angles occur during the three fast latitude scans around 1995, 2001 and 2007. Here, Ulysses’ distance to Sun and Earth is at a minimum.

The variable aspect angle is incorporated into the analysis by rotating the field of view corresponding to  $\varphi_{asp}$  and  $\vartheta_{asp}$ . This results in a likewise rotation of the velocity acceptance space. In fig. 3.8 the acceptance velocity for a single absolute velocity  $v = 600 \text{ km s}^{-1}$  is shown for  $\varphi_{asp} = 25^\circ$  and  $\vartheta_{asp} = -10^\circ$ . Note, that the orientation here seems to be mirrored against the convention that has been described before. This is due to the inversion when transitioning from the field of view to velocity acceptance, s. eq. 3.1.

When comparing fig. 3.8 with fig. todo(v acceptance ohne AA!), where a situation with  $\vartheta_{asp} = \varphi_{asp} = 0$  is shown, it becomes clear that especially larger aspect angles

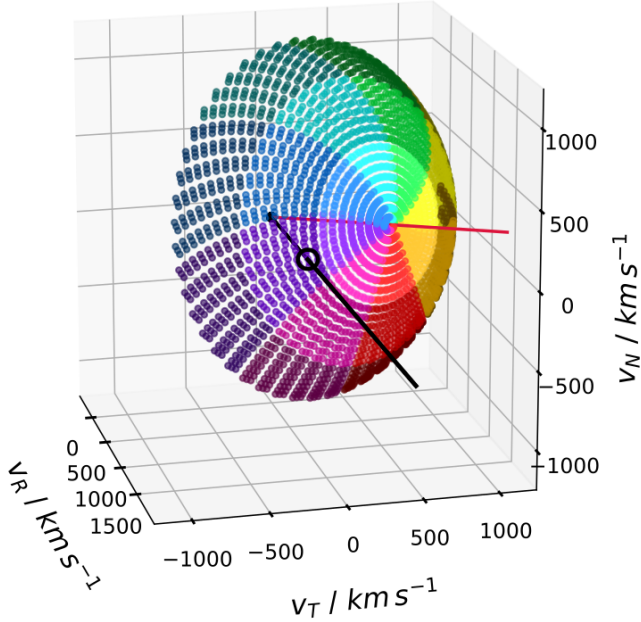


FIGURE 3.8: todo

change the link between a distinct sector-detector element and a volume in velocity space. While with a zero aspect angle a radial velocity (along  $\vec{R}$ ) would be detected right in the middle of the velocity shell and definitely in the innermost detector, this is not the case for the aspect angle in fig. 3.8. Here, an exclusively radial oriented velocity would be detected in a distinct sector in the central detector.

This also means that we can only transform a sector-detector measurement into a position in velocity space when we know about Ulysses' orientation!

### **Todo: steps asp Winkel**

#### **Consistency Check**

For checking if the considerations made before are reasonable and if the virtual detector works in the right way, we want to take a look at data of which we believe to know the velocity distribution function. Appropriate test data is the solar wind itself as it is believed to flow radially outwards from the Sun (Prölss, 2004, ch. 6.1). An ideal candidate within the solar wind is  $\text{He}^{2+}$  as the most abundant species. We can identify  $\text{He}^{2+}$  easily in fig. 2.8 and are provided with good statistics. Unlike protons, which are even more abundant in the solar wind,  $\text{He}^{2+}$  most likely deposits energy above the detector's threshold in the solid-state detector (s. sec. 2.3.1). This is because of its higher mass and the twice as high charge, which leads to a higher gain in energy by the post acceleration. Only when a particle triggers an  $E_{\text{SSD}}$  measurement (Triple Coincidence) we get a directional information about its velocity. Protons are most often measured as Double Coincidences except for suprathermal protons, for which the assumption of radial stream must not hold true (Todo:Quelle. Lars?). For selecting  $\text{He}^{2+}$  we proceed like described in sec. 2.4.

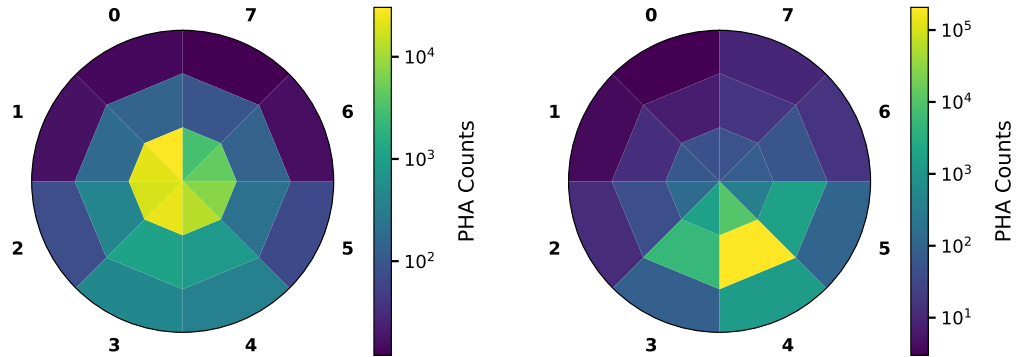


FIGURE 3.9: links: 1992, alle Tage aber AA eingeschränkt auf jeweils -5 bis 5 Grad; rechts: doy 1-90 aus 2001, AA nicht eingeschränkt

In a first step we look at periods of time in which both aspect angle components  $\varphi_{\text{asp}}$  and  $\vartheta_{\text{asp}}$  are small (Todo: genau?). For these nr\_todo PHA words we draw a histogram of their sector and detector information. The result can be seen in fig. todo. The histogram shows that mainly the innermost detector is hit. This is the expected behavior when we imagine the instrument on a spacecraft that points directly to the Sun. A radially streaming flow then hits the instrument's detector that is oriented sunwards, which does not change with the spin of the spacecraft. This result is also consistent with the detector model for  $\varphi_{\text{asp}} = \vartheta_{\text{asp}} = 0$  which is shown in fig. todo. A radial stream can be represented here by the black line which cuts through the velocity shell in its center, the region of the innermost detector, bla. Ir-gendwie schöner schreiben... (Due to the width... auf allen Sektoren?)

In a second step we examine a time period in which Ulysses had a substantial aspect angle. This is particularly the case for when Ulysses is near its perihelion, s. fig 3.7. We choose for the second orbit, i.e. days 1-90 in 2001. For all  $\text{He}^{2+}$  PHA data from this time we again histogram sector and detector information, which is shown in fig. 3.9. Compared to fig. todo the maximum of counts is now shifted clearly towards a single sector, that is sector No. 4, and the central detector. This is consistent with the virtual detector in fig. 3.8, where the aspect angle's quantity matches the one in the selected time period. Counts do not show up exclusively with this single sector-detector combination but slightly spread out over adjacent sector-detector elements. This is due to the fact that solar wind  $\text{He}^{2+}$  does not stream as an ideal beam but has a certain temperature, i.e. width (Prölss, 2004, ch. 6.1).

### TODO: Sunpulse Trigger – Rotation

In the previous section it was observed that  $\text{He}^{2+}$  PHA counts accumulate around the central detector for large aspect angles. Still it needs to be examined, in which sector counts are concentrated.

As mentioned before, one spacecraft spin is divided into 8 sectors, starting with sector 0 and ending with sector 7. Every spin's start is defined newly by the “spin reference pulse” of Ulysses (Hunt-Ward and Armstrong, 1999). This pulse is triggered by a combination of four sun sensors which detect when the Sun crosses a plane that is spanned by the spacecraft's spin axis and the spacecraft's X-axis, which

is a particular axis perpendicular to the spin axis. The spin reference pulse is not uniform over time as the position of the Sun relative to the spacecraft changes with varying aspect angle.

To extract correct directional information from a sector data product of an ion that has been detected by SWICS it is essential to know the relative orientation between SWICS' main axis and the X-axis on the spacecraft. In the virtual detector this is implemented as an angle against the spacecraft–Sun line by which the field of view is rotated around the spin axis.

From the SWICS DPU (1988, S.20-22) we know that with “normal orientation” the sun pulse occurs in the center of SWICS sector 4, which implies a  $180^\circ$  offset between the spacecraft–Sun line and SWICS sector 0 (s. fig. 3.10 for clarification). However, it was possible to set a fine adjustment which would lead to an offset of the sun pulse from this center line up to  $22.5^\circ$  SWICS DPU (1988, S.48). Unfortunately, we do not know about the value that has been chosen.

If we assumed a wrong angle, a particle beam coming from a fixed direction in a Sun-fixed frame would be linked to a different direction. But this shift between true and supposedly measured direction is not constant over aspect angles. If we then measured over a longer time period with various aspect angles, we would measure the beam as blurred in velocity space.

To make sure our model uses the right angle, we again choose  $\text{He}^{2+}$  as a test population of which we assume a beam-like behaviour streaming radially from the Sun. Also, we can only look at time periods when the aspect angles were large and the maximum of  $\text{He}^{2+}$  counts occurs in the central or outermost detector. Only here we can clearly discriminate between single sectors. When measured in the innermost detector the slightly widened distribution of  $\text{He}^{2+}$  would spread across all sectors as they are close together here. From fig. 3.9, right, where we histogrammed  $\text{He}^{2+}$  PHA words at a sizeably aspect angle, we find that the data is in agreement with the overall idea of a sun pulse in sector 4, when we believe the assumption that  $\text{He}^{2+}$  streams radially from the Sun. To check for a potential fine adjustment we search for tendencies of the maximum of counts sweeping to an adjacent sector. However, such a tendency that is consistent over time cannot be found. Thus, we proceed the analysis with the assumption that no crucial fine adjustment had been set.

**Todo :** Hier oder in den Ausblick? Sollte man nochmal in den Housekeepingdata checken und ggf. systematisch analysieren, ob das vielleicht daran liegt, dass  $\text{He}^{2+}$  doch nicht so radial strömt.

### Transformation into $w$ -space

With the considerations of eigen-velocity and orientation of Ulysses we can use the virtual detector for translating  $\text{He}^{2+}$  PHA words into the three dimensional velocity space. Only when we have unfolded absolute velocities into its three components we can take the important step of transforming from a spacecraft frame of reference to a solar wind frame of reference.

This can be done by subtracting the instantaneous solar wind speed in R-component from a velocity in the spacecraft frame (TODO: Annahme radiale Abströmung):

$$\mathbf{v}_{i,sw} = \begin{bmatrix} v_{R,i,sc} \\ v_{T,i,sc} \\ v_{N,i,sc} \end{bmatrix} - \begin{bmatrix} v_{sw} \\ 0 \\ 0 \end{bmatrix}$$

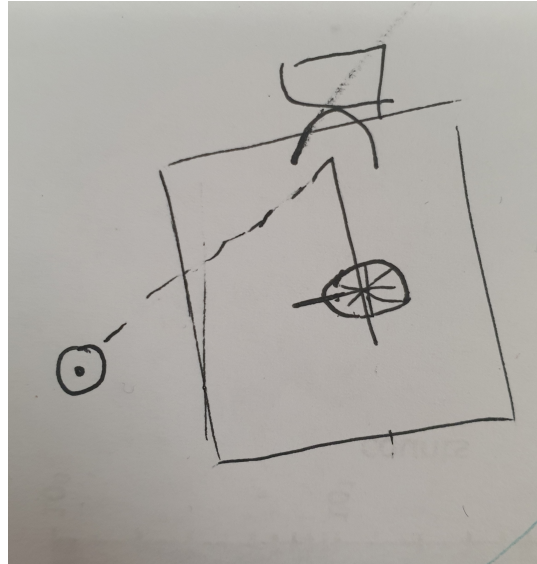


FIGURE 3.10: todo. Schemazeichnung Sunpulser-Problem

In a last step every component of the resulting vector is divided by solar wind speed:

$$\mathbf{w}_{i,sw} = \begin{bmatrix} v_{R,i,sw} \\ v_{T,i,sw} \\ v_{N,i,sw} \end{bmatrix} / \begin{bmatrix} v_{sw} \\ v_{sw} \\ v_{sw} \end{bmatrix}$$

By this, the transition from velocity space in the spacecraft frame to solar wind independent w space in solar wind frame of reference is made.

### 3.3 Velocity Distribution Function .....?

#### 3.3.1 Velocity Space Coverage

When analyzing He<sup>+</sup> PUI w-spectra with Ulysses SWICS, several effects have to be considered that limit the observable part of the w-space. The most obvious restriction results from the fixed geometry of the collimator (s. sec. 3.2.1)) which allows to observe only a dome-shaped part of the w-space when considering the spin of the spacecraft and varying ESA steps. (However, this dome is not fixed in w-space for different orientations of the spacecraft. While the ever changing aspect angle of Ulysses introduces a complex subject to directional data analysis it also enlarges the integrated coverage of velocity space over time.)

Furthermore, we have to deal with a limitation of the coverage in  $w_R$ -direction particularly for He<sup>+</sup> triple coincidences. The observable range in ESA steps is 19 to 0, which for He<sup>+</sup> corresponds to a limitation from 864 km s<sup>-1</sup> to 1708 km s<sup>-1</sup>. While the upper limit is simply due to SWICS' highest possible ESA step, the lower limit is the lowest value for which He<sup>+</sup> still has enough energy to overcome the threshold of the solid-state detector and thus can trigger a valid energy measurement (s. sec. 2.3.1).

The w-range that is consequently covered is highly dependent on the prevalent solar wind speed. For  $v_{sw} = 700$  km/s the absolute w in a spacecraft frame is limited to  $1.2 < w_{SC} < 2.4$ , whereas for slow solar wind at  $v_{sw} = 300$  km/s the limitation is

$2.9 < w_{SC} < 5.7$ . In fig. 3.11 an exemplary w-space coverage for  $v_{sw} = 700 \text{ km/s}$  and no aspect angle is sketched.

As we do not expect to measure the bulk of  $\text{He}^+$  at velocities  $w_{SC} \gg 2$ , we are thus limited to time periods with fast solar wind.

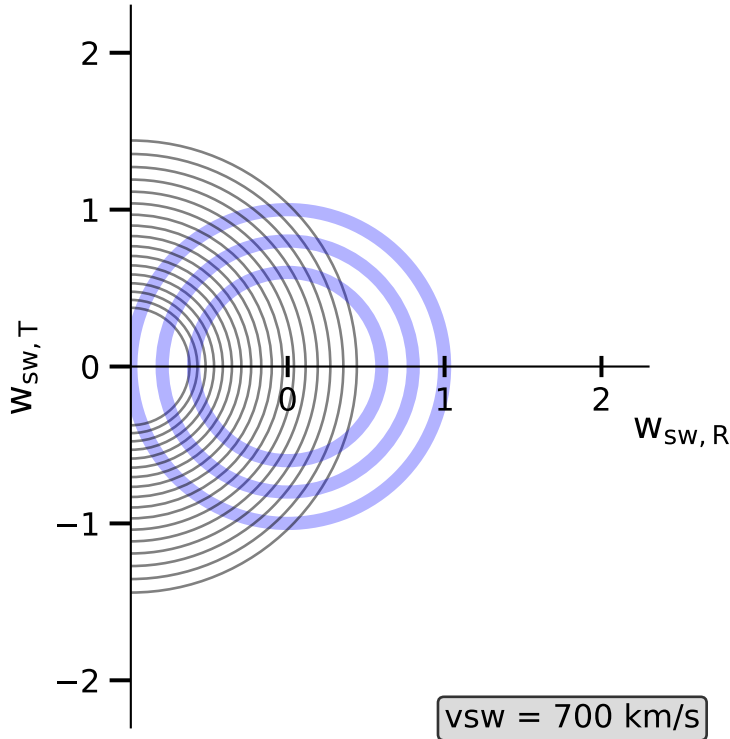


FIGURE 3.11: todo: Kollimatorbegrenzung einzeichnen. Nur ein Ring? Coverage ist falsch!!  
w im sw-frame!

In this work solar wind speed data is used that has been measured by the instrument SWOOPS (Solar Wind Observations Over the Poles of the Sun, Bame et al., 1992) on Ulysses.

In fig. 3.12 a histogram for occurring solar wind speeds is shown – limited to times in which  $\text{He}^+$  triple coincidences were measured. The number on the right indicates the total number of  $\text{He}^+$  PHA triple coincidence data that was received within the year. One can see the overall variation of the solar wind speed that is due to different latitudes of the spacecraft: When close to the poles of the Sun, Ulysses is exposed to the fast solar wind (McComas et al., 2004), which is the case for example in 1995. Also, the total number of received data decreases heavily towards years in which Ulysses approaches the orbit's aphelion, e.g. 1998 at the end of the first orbit. This is mainly an effect of pickup ion flux reduction that scales with  $r_\odot^{-2}$  due to the expansion of the solar wind (Prölss, 2004, ch. 6.1).

### 3.3.2 Phase Space Normalization

We are now able to combine the information about sector, detector and ESA step from the selected  $\text{He}^+$  PHA triple coincidences with the information about how the

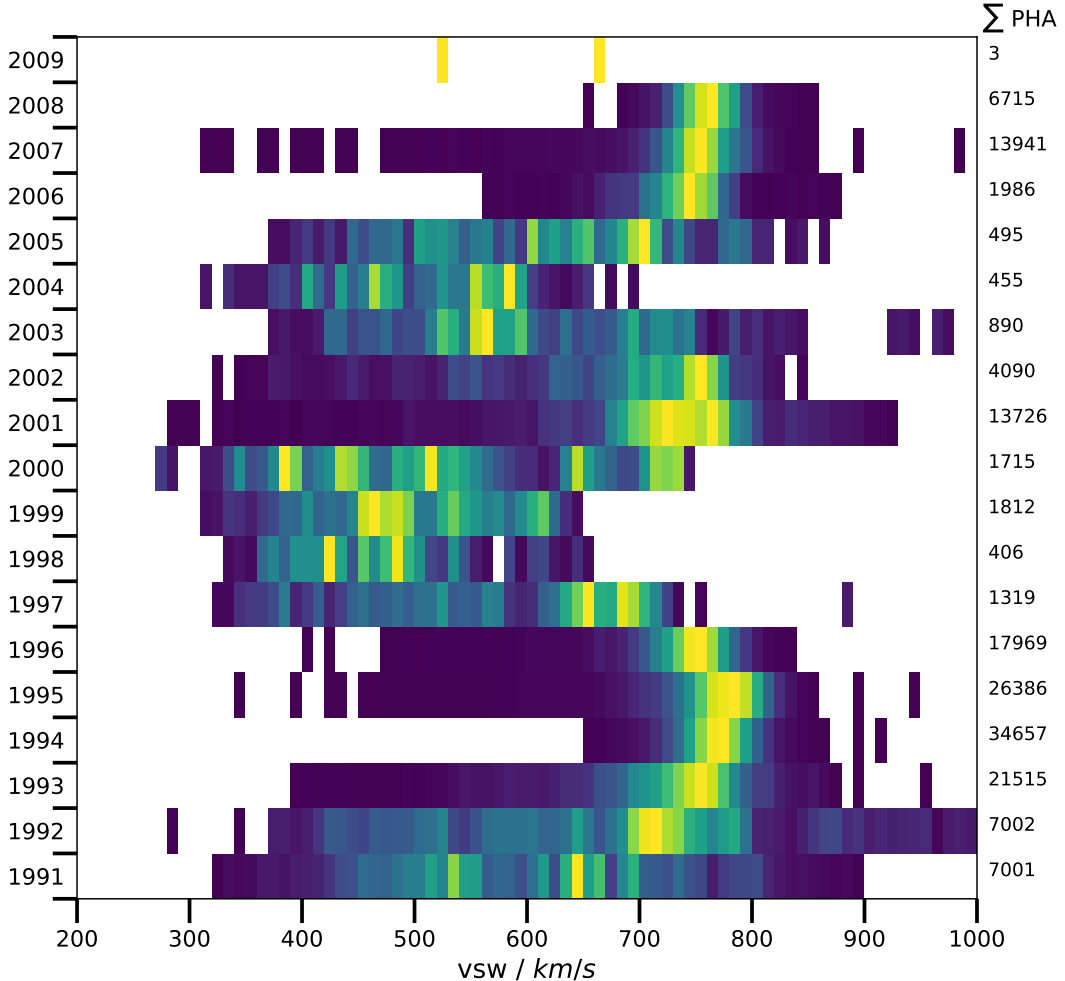


FIGURE 3.12: Histogram of solar wind speed measured by SWOOPS for times in which  $\text{He}^+$  PHA data is measured by SWICS, sorted by years of the Ulysses mission. The color code is normalized to each year's maximum value (in yellow). In the right column one can find the total number of  $\text{He}^+$  PHA words per year.

spacecraft was moving and which direction it was facing at the time of the measurement. Counts that we have collected over a certain time period can be mapped into three dimensional w-space by this. However, for deriving physical quantities from these, a transition from counts to phase space density has to be performed.

Firstly, we consider a single spin of the spacecraft, which normally corresponds to one ESA step of SWICS. Counts  $N_{jk}$  that have been measured in a phase space volume that has been covered by a sector-detector element  $j$  during the ESA step  $k$  can be connected to the average phase space density  $\delta_{jk}$  in this volume by an integration over the three dimensional velocity space:

$$N_{jk} = \iiint_{v_{\phi j} v_{\theta j} v_{Rk}} \rho_{jk} V_k d^3 v,$$

where  $V_k = G \tau v_k$  is the spatial volume of the measurement with the geometrical factor  $G = 0.0225 \text{ cm}^2$  (Dr. Lars Berger, personal communication),  $\tau = 12/8 \text{ s} =$

1.5 s, the time of the measurement in a single sector and  $v_k$  the central velocity for  $\text{He}^+$  in the ESA step  $k$ . With the opening angles of a single sector-detector element of  $4^\circ$  in width and  $69^\circ/3 = 23^\circ$  in length and the height of this element  $\Delta v_k$  we can write

$$N_{jk} = v_k^2 \left( \frac{\pi^2}{180^2} \cdot 4 \cdot 23 \right) \Delta v_k \rho_{jk} G v_k \tau.$$

$\Delta v_k$  is determined through the uncertainty in energy-per-charge measurement. It has been found to be  $\Delta v_k = 0.0125 v_k$  in sec. 3.2.1, which gives us

$$N_{jk} = v_k^4 \left( \frac{\pi^2}{180^2} \cdot 4 \cdot 23 \right) 0.025 \rho_{jk} G \tau.$$

This we can be rewritten as an expression for the average phase space density  $\delta_{jk}$  with the phase space volume  $V_k$  as

$$\rho_{jk} = \frac{N_{jk}}{V_k}.$$

Notice, that  $V_k$  is only dependent on the ESA step  $k$ , as the sector-detector elements span the same (absolute) phase space volume for one step.

When we want to measure more than one spin, we need to consider, that the probability to detect an ion is dependent on the ESA step. This behaviour is described in sec. 2.3.1 as the detection efficiency.

For phase space normalisation this is considered by weighting the spanned phase space volume for every sector detector element with the efficiency of the respective ESA step  $\text{eff}_k$ :

$$\rho_{jk} = \frac{N_{jk}}{V_k \cdot \text{eff}_k}$$

## T O D O:

Schreiben, dass das nur für kleine vsw-Fenster sinnvoll ist!

As the instrument covers different phase space volumes with varying aspect angle, changing parts of phase space volume are covered. However, we are actually interested in the average phase space density at a distinct volume element  $v_a$  in phase space. This we get by dividing the counts in the volume element  $v_i$  by the measured volume, both integrated over time and this volume. This means that we consider the time in which we could have measured bla...

$$\rho_{v_a} = \frac{\iint_{t v_a} N dv dt}{\iint_{t v_a} V \text{eff}_k dv dt}$$

Todo:

Schreiben, dass die velocity Akzeptanzpunkte mit den anteilmäßigen Counts histogrammiert werden? Vielleicht auch ins Data-Kapitel, weil das mit der Normierung gemacht wird...? Sind die Counts überhaupt durch n geteilt?

Im Folgenden benennen wir das (integriertes) PSV

## Chapter 4

# Results

Here we present first results of the method that has been developed in chapter 3 for  $\text{He}^+$ . For creating three dimensional velocity spectra from  $\text{He}^+$  SWICS PHA data we synchronize the selected data (s. 2,  $\text{He}^+$  Triple Coincidences) with the spacecraft's aspect angle, its eigen-velocity and the present solar wind speed. This gives us directionally resolved counts from the observed phase space volume.

An example for data of a measuring period of 50 days in 1993, limited to solar wind speeds from  $760 \text{ km s}^{-1}$  to  $780 \text{ km s}^{-1}$ , is shown in Fig. 4.1. Here we histogrammed the counts by utilizing Cartesian  $w_{\text{sw},R}$ ,  $w_{\text{sw},T}$  and  $w_{\text{sw},N}$  bins in solar wind frame. Shown are counts from a "slice" in the  $w_{\text{sw},T} - w_{\text{sw},N}$  plane. Counts within the range  $0.3 \leq w_{\text{sw},R} < 0.5$  have been summarized for each  $w_{\text{sw},T} - w_{\text{sw},N}$  bin. The orientation of this cut is sketched in Fig. 4.2 for better understanding.

By dividing these counts by the integrated phase space volume (PSV) for the ob-

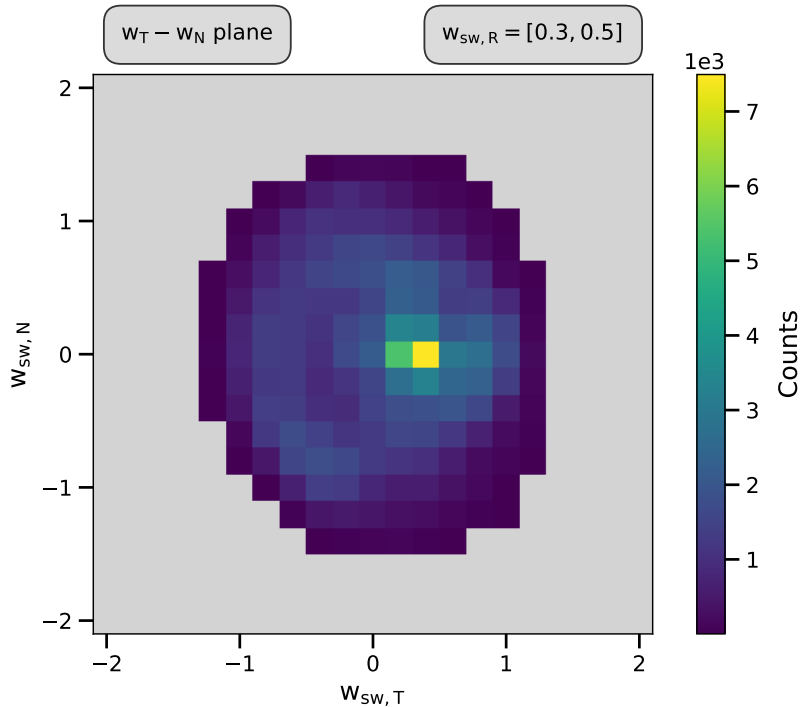


FIGURE 4.1: Cartesian cut through  $\text{He}^+$  count distribution in a 3D  $w_{\text{sw}}$ -space, measured during DOY 315-365 in 1993 for solar wind speeds from  $760 \text{ km s}^{-1}$  to  $780 \text{ km s}^{-1}$ .

served time, which is binned in the same way and shown in Fig. 4.3, we yield the resulting phase space density (PSD), s. Fig. 4.4. When comparing the three figures

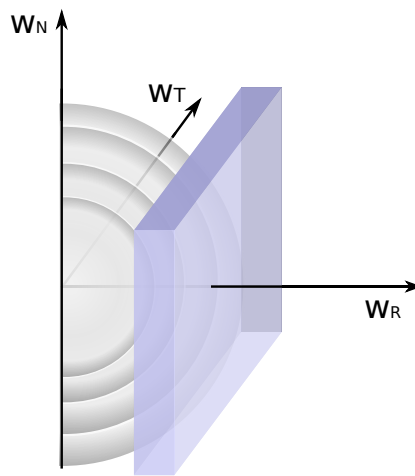


FIGURE 4.2: Sketch of the orientation of a slice in the  $w_T - w_N$  plane.  
A selection of ESA shells is shown in grey.

[4.1](#), [4.3](#) and [4.4](#) one can see a clear difference in overall shape between PSV and PSD (resp. counts). The nonzero part of the PSD does not cover all of the scanned PSV. This means that SWICS did not observe He<sup>+</sup> PUI over all of the observed PSV but only in a distinct partial volume.

However, the 2D projection of the PSD has a roundish shape. In fact we even find a spherical shape in 3D. As a feasible visualization a stepwise sequence of  $w_{sw,T} - w_{sw,N}$  “slices” is displayed in the appendix [A](#). Each slice is again a projection of the PSD from a width  $\Delta w_{sw,R} = 0.2$ . The sequence starts with  $w_{sw,R}$ -values below solar wind speed with the slice  $-0.5 \leq w_{sw,R} < -0.3$  and steps seamlessly up to  $1.1 \leq w_{sw,R} < 1.3$  in nine increments. The radius of the projection increases slightly towards  $w_{sw,R} \approx 0$  and then starts decreasing again for larger  $w_{sw,R}$ . This suggests the three dimensional shape of a sphere centered around  $w_{sw,R} = 0$ , which is a finding that confirms TODO.

For  $w_{sw,R} < 0$  and towards smaller values of  $w_{sw,R}$  an increasing “hole” in the PSD emerges from the center. This is due to the fact of a limited instrumental coverage for He<sup>+</sup> at higher ESA steps, which is described in more detail in sec. [3.3.1](#).

Apart from taking slices from the  $w_{sw,T} - w_{sw,N}$  plane along the  $w_{sw,R}$ -axis we can also cut the three dimensional distribution of the PSD along the other two axes. This is shown for the  $w_{sw,R} - w_{sw,N}$  plane in Fig. [4.5](#) and for the the  $w_{sw,R} - w_{sw,T}$  plane in Fig. [4.6](#), each projection containing  $w_{sw,R} = 0$ . Both images confirm the underlying three dimensional spherical distribution.

Taking a look at the  $w_{sw,R}$ -slice of the PSD in Fig. [4.4](#) again, one sees a relatively sharp peak in the bins around  $w_{sw,T} = 0.4$  and  $w_{sw,N} = 0$ . This means that this part of PSV has been observed more often than surrounding parts, which is due to the spacecraft having a substantial aspect angle  $\varphi_{asp}$  at the end of the year 1993 (s. Fig. [3.7](#)). Because the spacecraft’s spin axis was tilted away from the radial direction for most of the time, this peak is shifted a little bit away from the center. The fact that this distinct part of PSV has been observed particularly often is followed by a qualitatively similar peak in counts, s. Fig. [4.1](#). As this peak is a result of the measurement and not a feature in the velocity distribution of He<sup>+</sup>, it vanishes with the normalization process. The PSD shows an increased density over a wider range around the radial direction, which tells that He<sup>+</sup> tends to stream radial in this example from 1993.

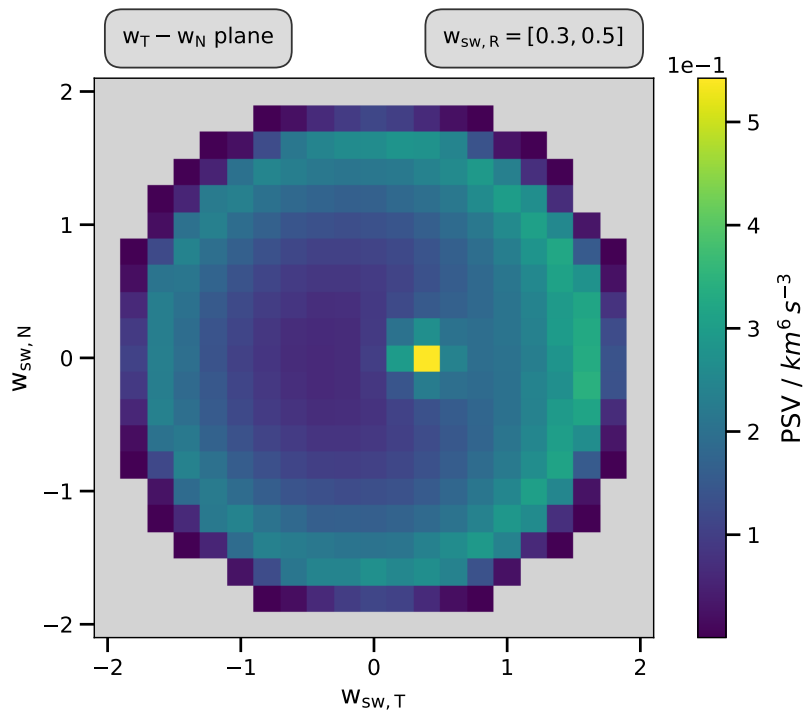


FIGURE 4.3: Cartesian cut through the integrated observed PSV in a 3D  $w_{sw}$ -space, measured during DOY 315-365 in 1993 for solar wind speeds from  $760 \text{ km s}^{-1}$  to  $780 \text{ km s}^{-1}$ .

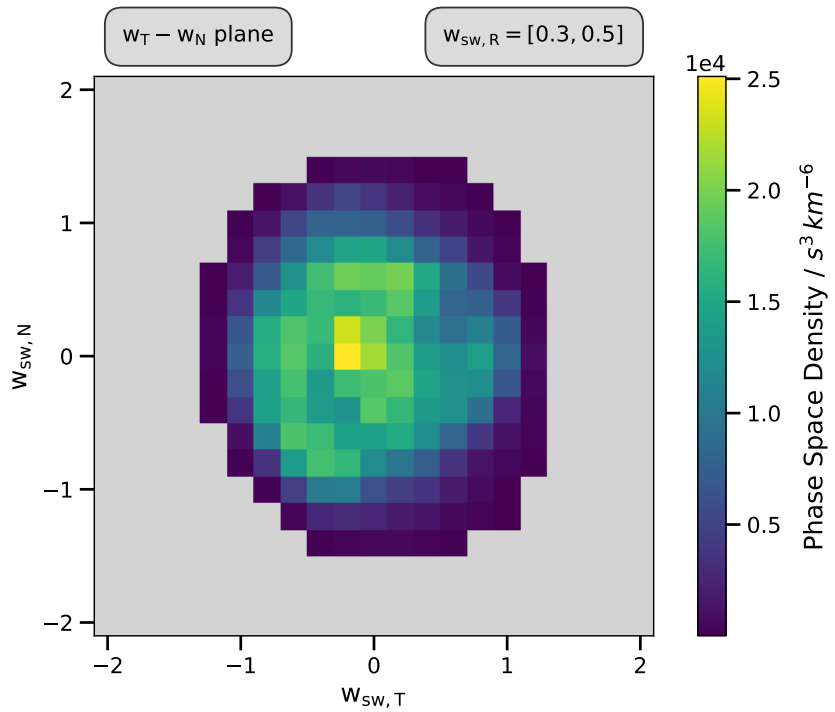


FIGURE 4.4: Cartesian cut through the three dimensional PSD for  $\text{He}^+$ , measured during DOY 315-365 in 1993 for solar wind speeds from  $760 \text{ km s}^{-1}$  to  $780 \text{ km s}^{-1}$

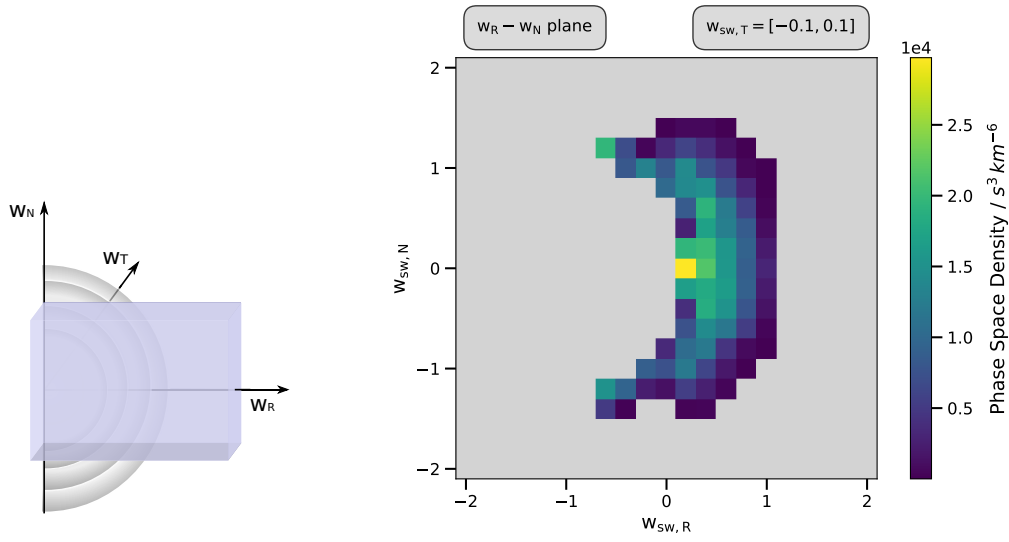


FIGURE 4.5: **Left:** Sketch of the orientation of a slice in the  $w_R - w_N$

plane. A selection of ESA shells is shown in grey.

**Right:** Cartesian cut through the three dimensional PSD for  $\text{He}^+$ , measured during DOY 315-365 in 1993 for solar wind speeds from  $760 \text{ km s}^{-1}$  to  $780 \text{ km s}^{-1}$ . The crescent shape results from SWICS' coverage.

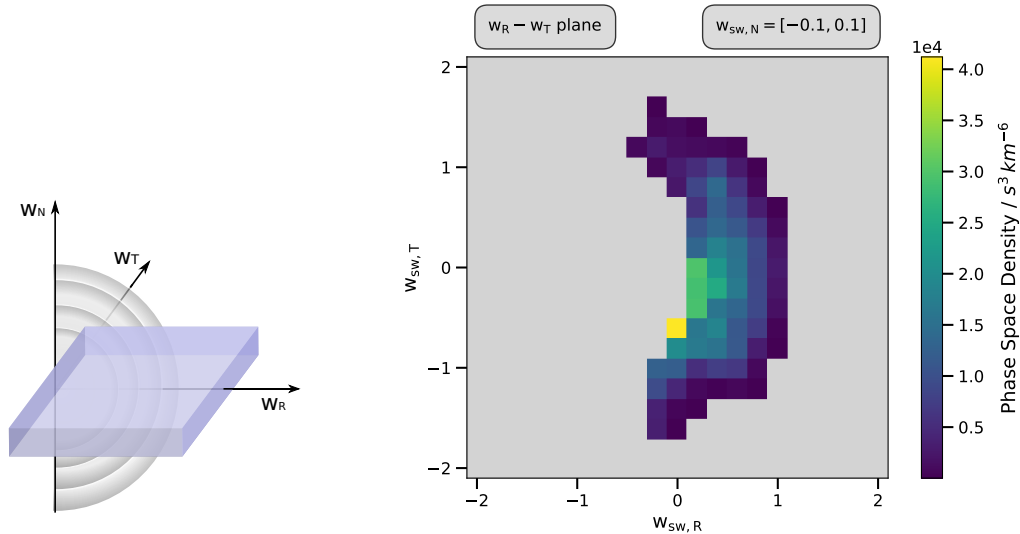


FIGURE 4.6: **Left:** Sketch of the orientation of a slice in the  $w_R - w_T$  plane. A selection of ESA shells is shown in grey.

**Right:** Cartesian cut through the three dimensional PSD for  $\text{He}^+$ , measured during DOY 315-365 in 1993 for solar wind speeds from  $760 \text{ km s}^{-1}$  to  $780 \text{ km s}^{-1}$ . The crescent shape results from SWICS' coverage.

In Fig. 4.9 we show the PSD for another longer time period of 250 days in 1994 at solar wind speeds  $740 \text{ km s}^{-1}$  to  $780 \text{ km s}^{-1}$  for a slice  $0.1 \leq w_{\text{sw},R} < 0.3$ . Corresponding Counts and PSV are shown in Fig. 4.7 and 4.8. Here, the counts show a ring structure which vanishes by normalization. The PSD in Fig. 4.9 shows distribution similar to the PSD from the shorter time period in 1993, concentrated and symmetrical around the central radial direction.

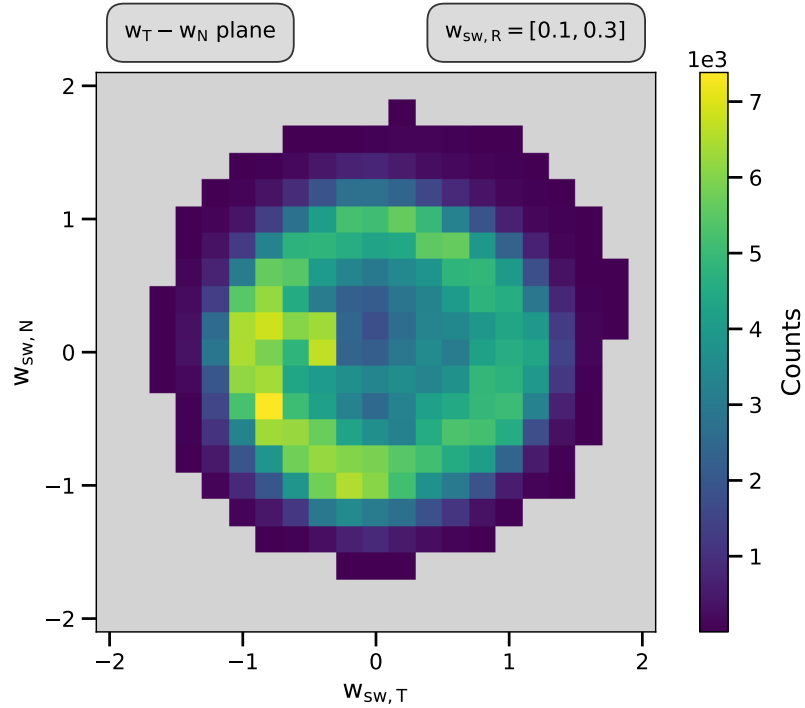


FIGURE 4.7: Cartesian cut through  $\text{He}^+$  count distribution in a 3D  $w_{\text{sw}}$ -space, measured during DOY 1-250 in 1994 for solar wind speeds from  $740 \text{ km s}^{-1}$  to  $780 \text{ km s}^{-1}$ .

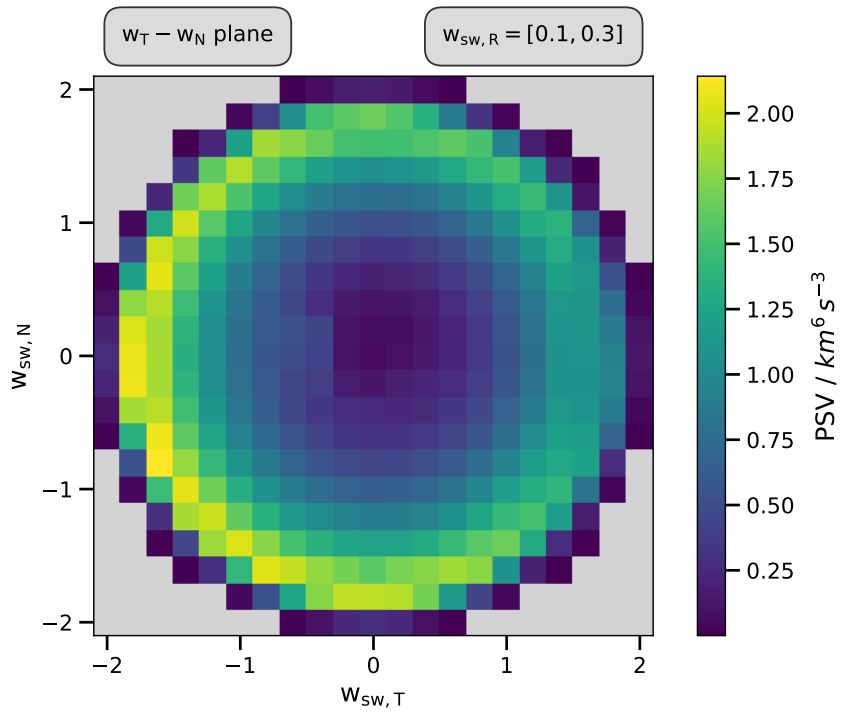


FIGURE 4.8: Cartesian cut through the integrated observed PSV in a 3D  $w_{sw}$ -space, measured during DOY 1-250 in 1994 for solar wind speeds from  $740 \text{ km s}^{-1}$  to  $780 \text{ km s}^{-1}$ .

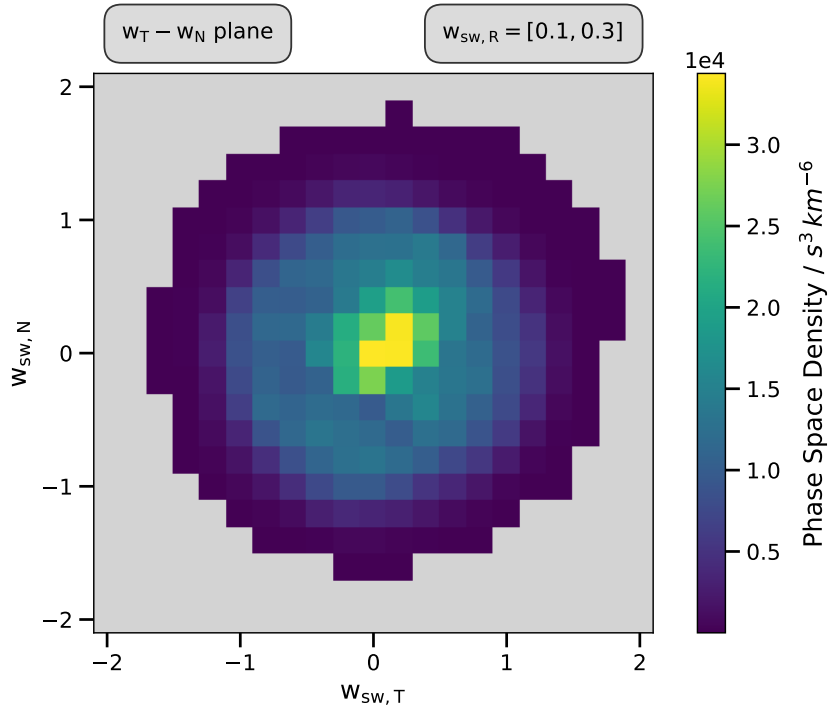


FIGURE 4.9: Cartesian cut through the three dimensional PSD for  $\text{He}^+$ , measured during DOY 1-250 in 1994 for solar wind speeds from  $740 \text{ km s}^{-1}$  to  $780 \text{ km s}^{-1}$

## 4.1 Spherical Projection

Of course we are not limited to the presented Cartesian projections. We can also choose a shell-wise projection. For this we consider spherical shells of constant  $w_{sw}$  in the solar wind frame. For better understanding we can refer to Fig. 3.11 again. Here we see the blue rings as 2D cuts through such concentric shells around  $w_{sw} = 0$ . The spherical coordinate  $\varphi$  is measured within the  $w_{sw,T} - w_{sw,N}$  plane with  $\varphi = 0^\circ$  for  $w_{sw,T} = 0$  and  $\varphi > 0^\circ$  for negative values  $w_{sw,T}$ . The second coordinate  $\vartheta$  is defined perpendicular to the  $w_{sw,T} - w_{sw,N}$  plane. It is  $\vartheta = 0^\circ$  for values within the plane and  $\vartheta = 90^\circ$  along the positive  $w_{sw,N}$  axis (out of the paper plane). In Figs. 4.10 and 4.11 we show counts and integrated PSV in this projection for He<sup>+</sup> measurements from 50 days in 1993, restricted to solar wind speeds from 760 km s<sup>-1</sup> to 780 km s<sup>-1</sup>. The selected spherical shell comprises absolute  $w$ -values  $0.85 \leq w_{sw} < 0.95$ . Considering the definition of the two coordinates  $\varphi$  and  $\vartheta$  we find, that the central viewing direction against the  $w_{sw,R}$  axis in Fig. 3.11. Even more clearly than in the Cartesian projection sharp peaks around  $\varphi = 30^\circ$  and  $\vartheta = 0^\circ$  are apparent in both figures 4.10 and 4.11, which is due to the variation in observation time of PSV. The histogram of the corresponding PSD, that excludes this effect, is shown in figure 4.12.

This spherical projection can become particularly suitable for the examination of the level of isotropy within a  $w_{sw}$ -shell. Shapes like a torus distribution (TODO ref PUI Kapitel) can be observed directly. For a completely isotropized shell we would expect an evenly colored projection in Fig 4.12. This is obviously not the case. Here, we find a structure of increased PSD that is around  $-60^\circ$  longitude for  $\vartheta = 0^\circ$  and moves towards  $\varphi = 0^\circ$  for higher latitudes.

Unfortunately, we could not find clear structures that were constant over different periods of measurement. A possible reason for that could be that we could only very vaguely determine the detection efficiency in sec. 2.3.1. As the spherical projection comprises measurements from different ESA steps (s. 3.11), an inaccurate efficiency weighting could either lead to a disappearance of real structures or even to an emerging of artificial ones. A detailed analysis of the detection efficiencies as it is shown in Köten (2009) for ACE/SWICS is beyond the scope of this work but would be highly beneficial for future analyses.

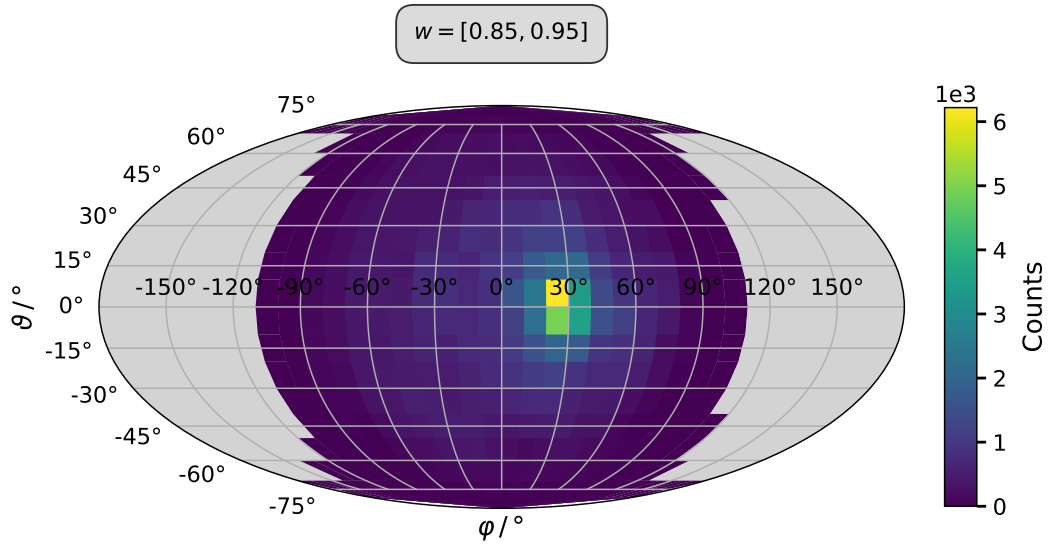


FIGURE 4.10: Spherical projection of  $\text{He}^+$  count distribution in a 3D  $w_{\text{sw}}$ -space, measured during DOY 315-365 in 1993 for solar wind speeds from  $760 \text{ km s}^{-1}$  to  $780 \text{ km s}^{-1}$ . Grey areas depict PSV that has not been observed and result from SWICS' coverage.

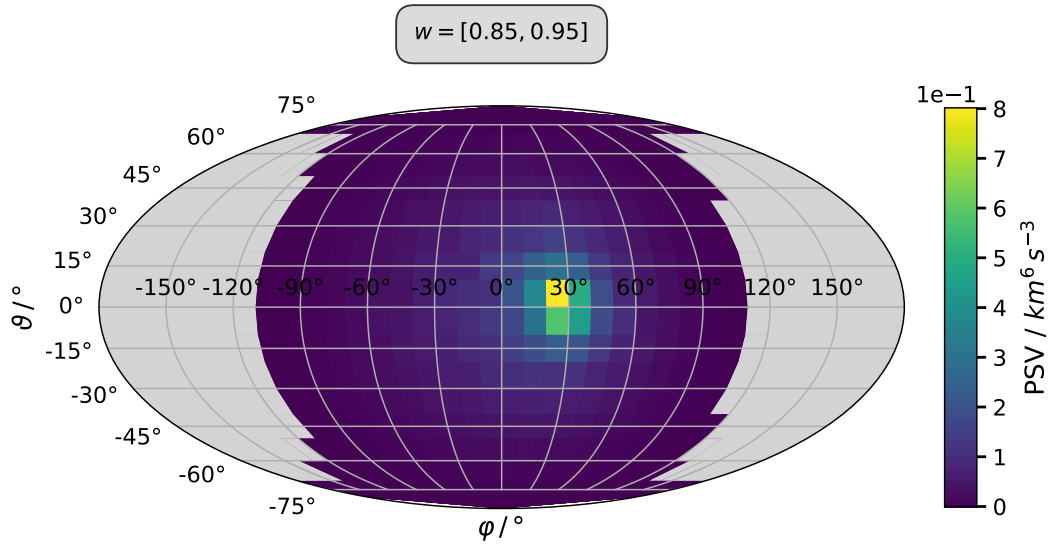


FIGURE 4.11: Spherical projection of the integrated observed PSV in a 3D  $w_{\text{sw}}$ -space, measured during DOY 315-365 in 1993 for solar wind speeds from  $760 \text{ km s}^{-1}$  to  $780 \text{ km s}^{-1}$ . Grey areas depict PSV that has not been observed and result from SWICS' coverage.

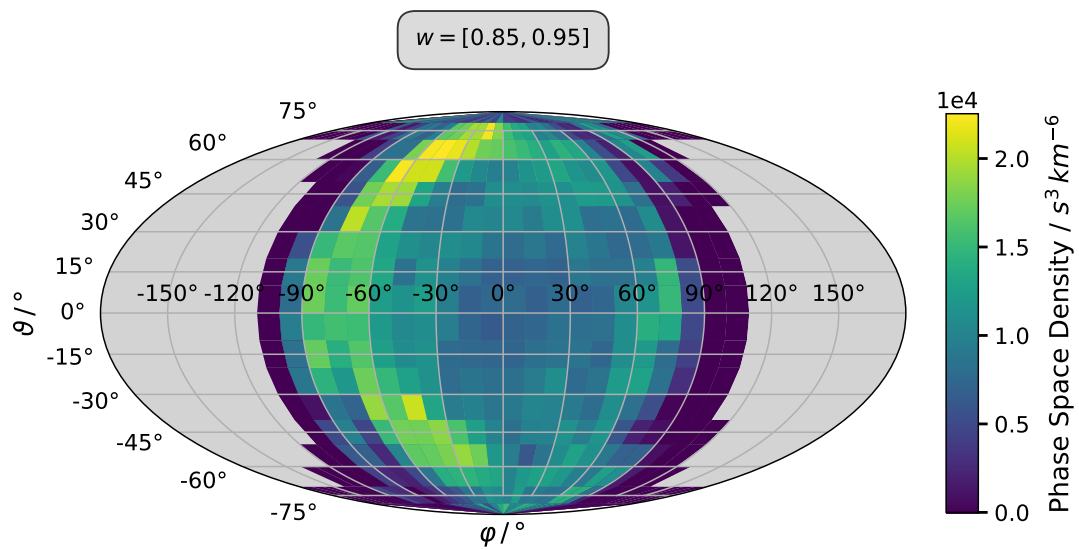


FIGURE 4.12: Spherical projection of the three dimensional PSD for  $\text{He}^+$ , measured during DOY 315-365 in 1993 for solar wind speeds from  $760 \text{ km s}^{-1}$  to  $780 \text{ km s}^{-1}$ . Grey areas depict PSV that has not been observed and result from SWICS' coverage.

## 4.2 1D Projection

In this last section we show 1D projections of three dimensional velocity distributions from measurements of two different years. In each year (1994, 1996) we analyzed  $\text{He}^+$  data from 100 days at solar wind speeds from  $760 \text{ km s}^{-1}$  to  $770 \text{ km s}^{-1}$ . For this projection we integrate both the counts and the PSV over spherical shells around  $w_{\text{sw}} = 0$ . In a 2D cut this can be visualized by an integration along a blue circle in Fig. 3.11. We combined values within the width  $\Delta w_{\text{sw}} = 0.1$  at different radii from  $w_{\text{sw}} = 0.25$  to  $w_{\text{sw}} = 1.05$ . In Fig. 4.13 the histogram of the resulting PSD is shown. The histograms look qualitatively similar for both years. We see a relatively broad distribution with a clear cutoff around  $w = 1$ , which corresponds to  $w_{\text{sc}} = 2$  (Todo: Verweis PUI Kapitel). For smaller values of  $w_{\text{sw}}$  the distribution does not change over many magnitudes.

The spectra in Fig. 4.13 are also in good qualitative agreement with the one in Fig.(todo:gloeckler). It should be noted that our spectra are limited to values  $w_{\text{sw}} > 0.25$ , while the spectrum in todo is continued down to values  $w_{\text{sc}} < 1$ , which corresponds to values  $w_{\text{sw}} < 0$  in solar wind frame. In sec. 3.3.1 we have seen that  $\text{He}^+$  Triple Coincidences can only be measured for distinct  $w$ -values above a limit that is dependent on the solar wind speed but hardly smaller than  $w_{\text{sw}} = 1$ . This shows that the spectrum in Fig.(todo:gloeckler) is not based on solely Triple Coincidences but also on  $\text{He}^+$  Double Coincidences. As Double Coincidences lack an energy measurement in the solid-state detector and thus a directional resolution, the spectrum can only result from an integration along different ESA shells that is projected onto a distinct possible value. Although the spectra look similar we want to emphasize that the spectrum in Fig. 4.13 results from a very different approach as we show projected cuts through an actual three dimensional velocity distribution.

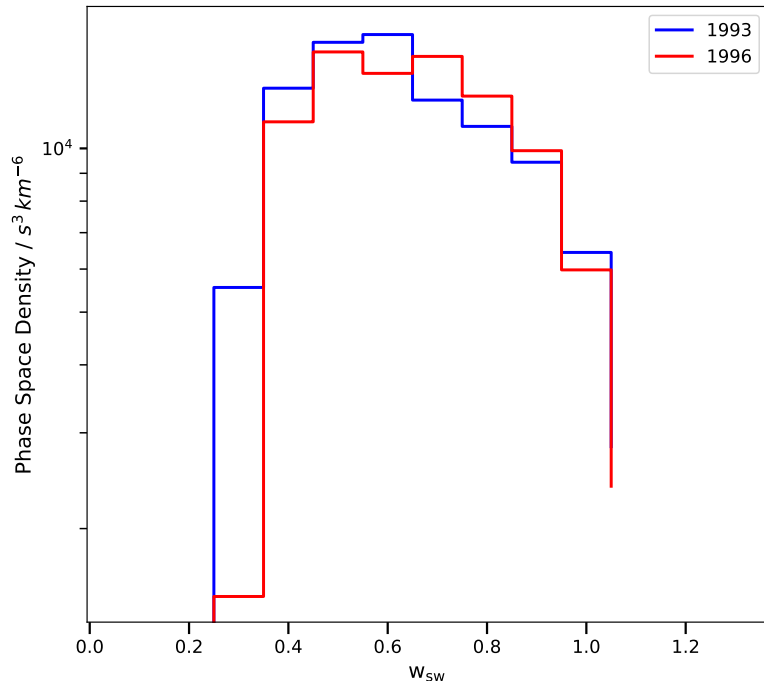


FIGURE 4.13: 1D projected PSD from a 3D  $w_{\text{sw}}$ -space, measured during DOY 1-100 in 1994 and 1996 for solar wind speeds from  $760 \text{ km s}^{-1}$  to  $770 \text{ km s}^{-1}$

## Chapter 5

# Summary and Outlook

The aim of this work was to prepare a tool for resolving ion measurements by Ulysses/SWICS in three dimensions and to apply this tool using He+ PUI.

In a first step He+ data was selected from the raw Ulysses SWICS PHA data. He+ events were identified by analyzing SWICS' combined measurements of energy-per-charge, time-of-flight and residual energy.

In a second step a model of the SWICS detector was developed, which allows us to translate the PHA data into three dimensional velocity components. Here the key point was to combine the PHA data with the complex geometry of SWICS' entrance system and the trajectory data of Ulysses. For realizing this, a virtual detector, following the original geometry of SWICS, was built in Python. The detector's velocity acceptance was reconstructed in multiple steps. While the absolute velocity of He+ ions followed from the energy-per-charge information, three dimensional components were obtained by SWICS' sector- and detector resolution. For the correct interpretation of these it was significant to consider the instrument's orientation. After having calculated this from data of Ulysses' and the Earth's orbit we were able to incorporate the spacecraft's aspect angle, SWICS' Orientation within the spacecraft's spin and Ulysses' eigen-velocity for every point in time.

After a consistency check with solar wind He2+ we were able to translate He+ Triple Coincidences into three dimensional velocity components. A phase space normalization was necessary for translating counts into the physically relevant quantity phase space density. Finally, we presented three dimensional velocity distributions using different projections.

These newly created three dimensional data products can significantly contribute to a better understanding of PUI phase space transport. By the deconvolution of former 1D velocity spectra into directionally resolved spectra the evolution of the PUI VDFs can be studied in detail. Existing theory on processes that shape these distributions like cooling mechanisms and pitch-angle scattering can be tested directly. Ulysses' outstanding orbit that spans a wide range of solar radii particularly suggest exploring the radial evolution of these processes.

In future, the presented method could also be adapted to other PUI than He+, e.g. O6+ or He2+ – or even to solar wind ions.

In this work we could already confirm with our super duper method that He+ PUI feature sphere-like VDF.

In this work we decided for He+ PUI as a first approach for our method. Die hier vorgestellte Analyse wurde exemplarisch an He+ PUI durchgeführt und es konnten erstmalig von SWICS gemessene 3d VDF präsentiert werden.

(vorher: nur Betrag. Jetzt: Komponenten).

**Restrictions:**

Auflösung eingeschränkt

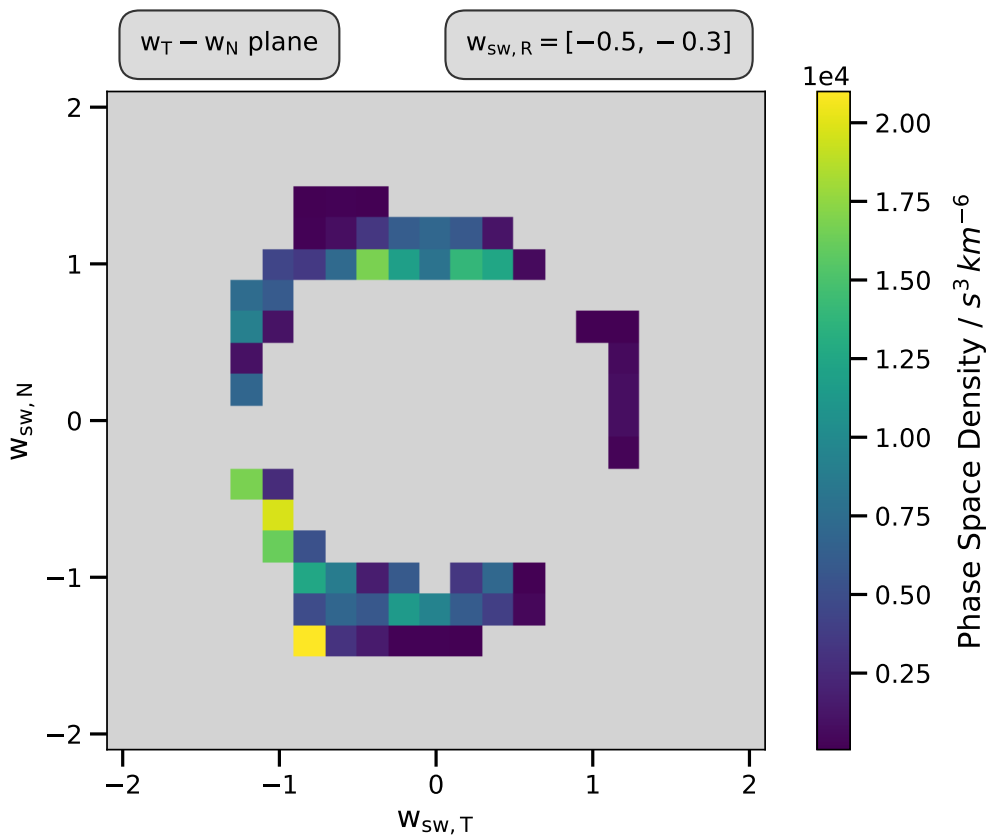
Wir sind eingeschränkt auf schnellen SW

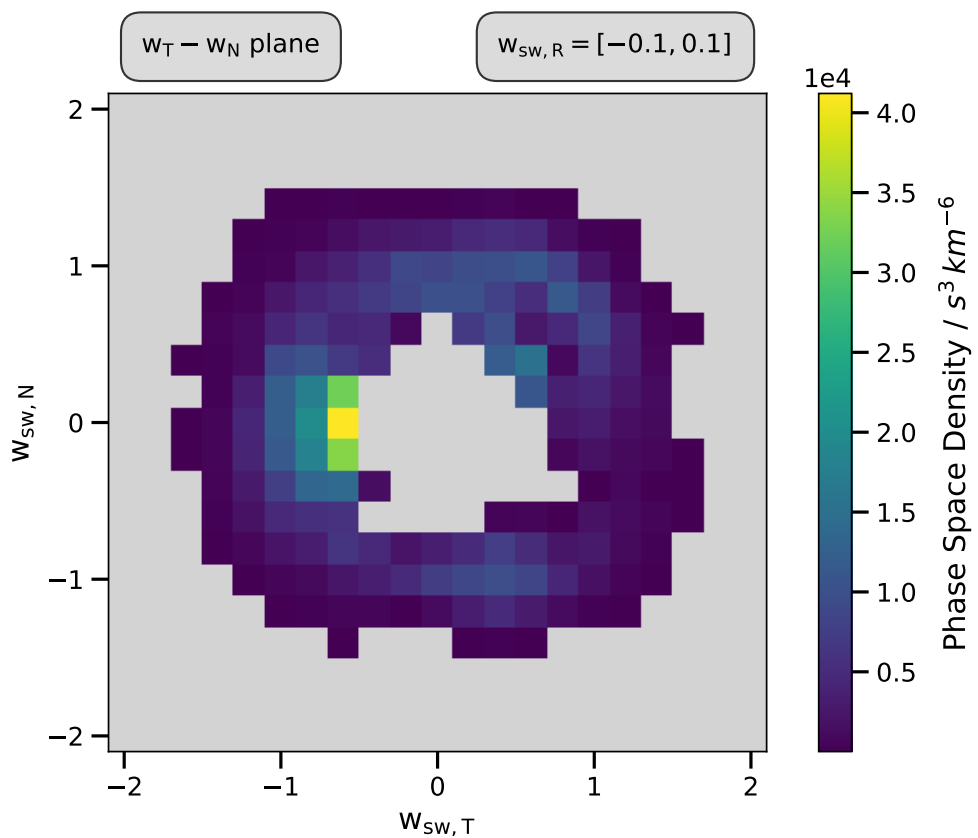
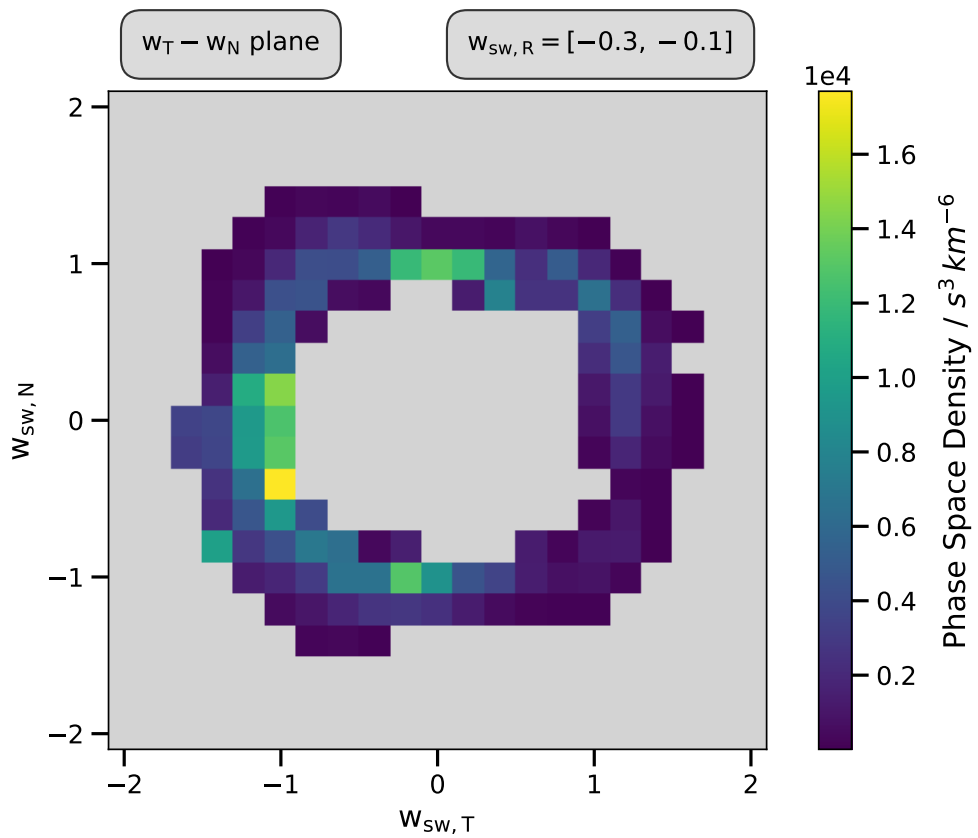
assumption: vsw nur radial

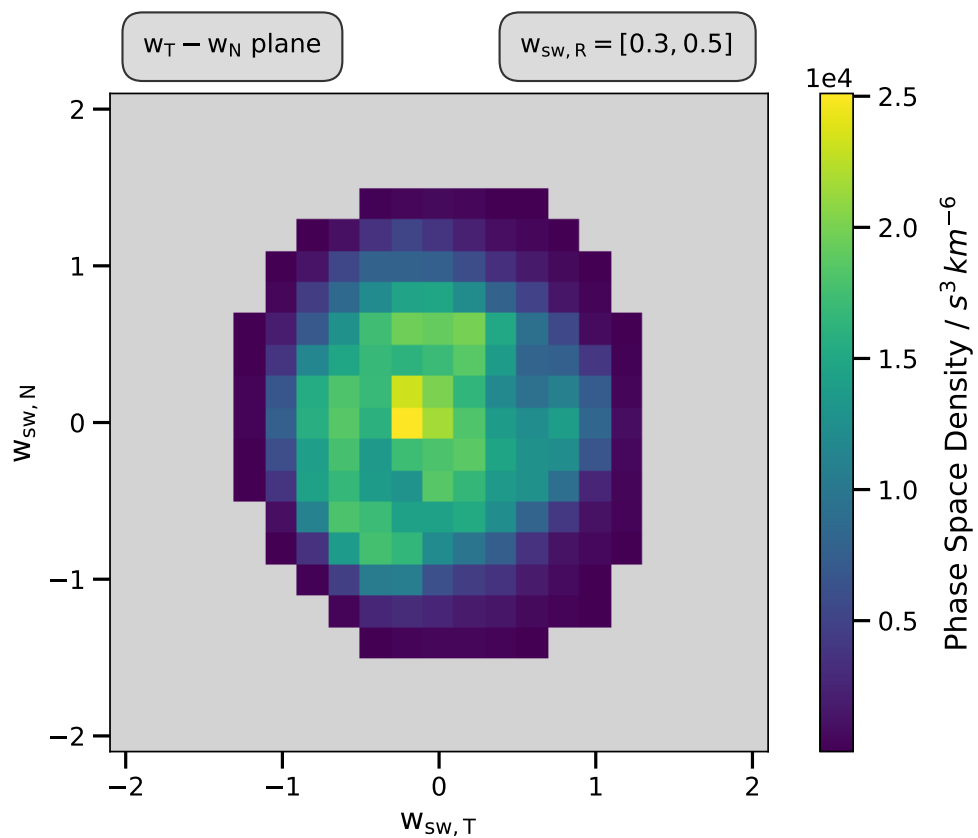
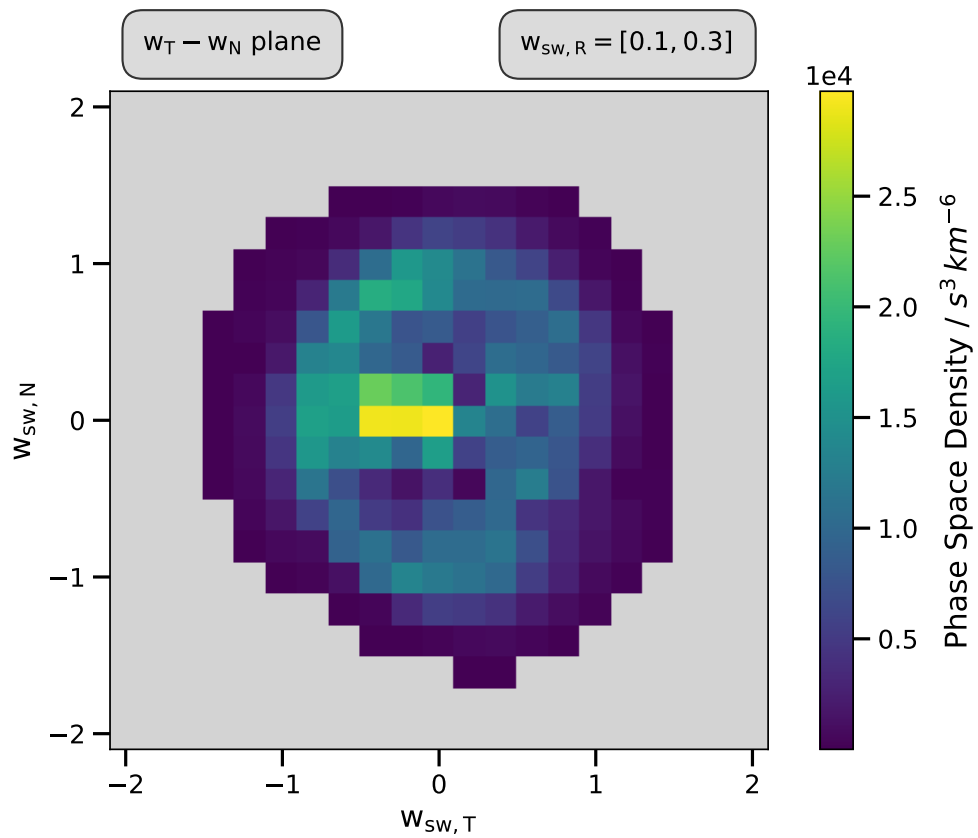
Efficiency müsste genau bestimmt werden: Dabei berücksichtigen, welcher Anteil unter den Threshold wandert. Evtl. überschätzen wir die Eff., wenn wir die interpolierten Werte von ACE/SWICS nehmen.

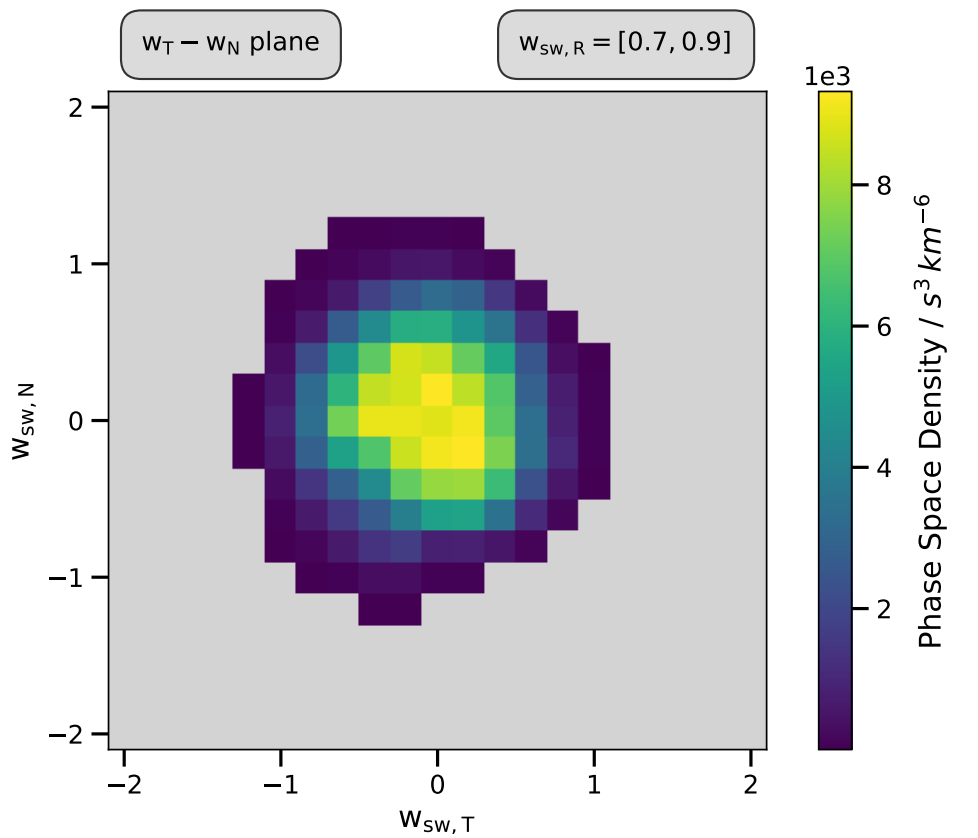
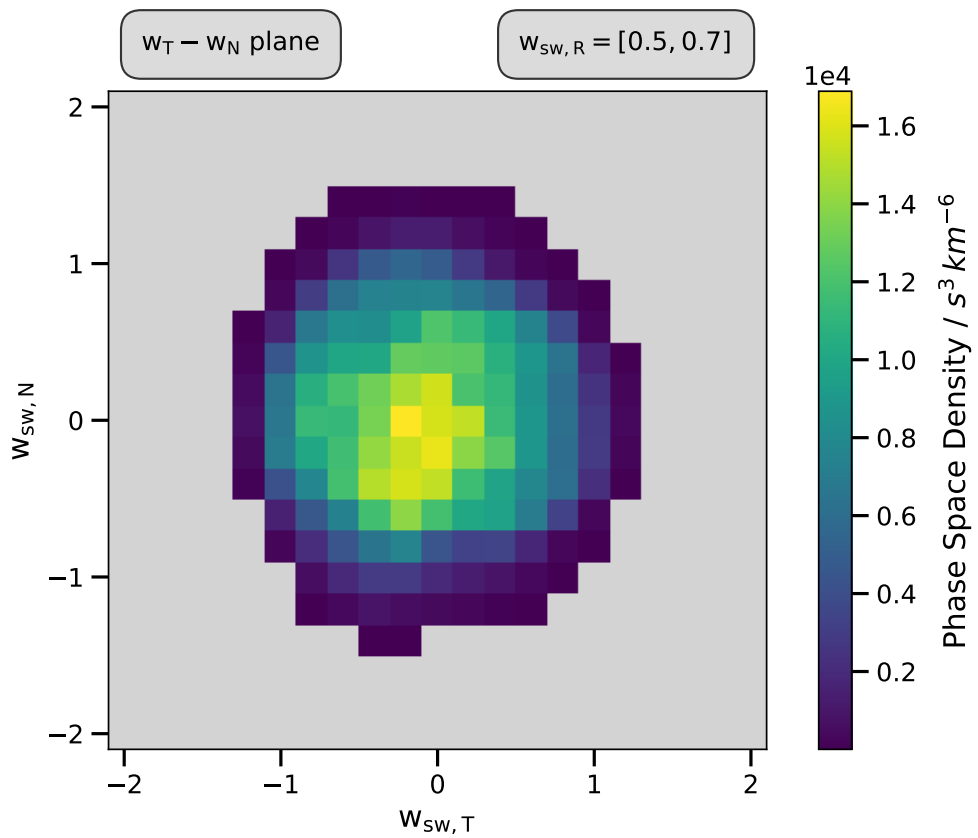
## Appendix A

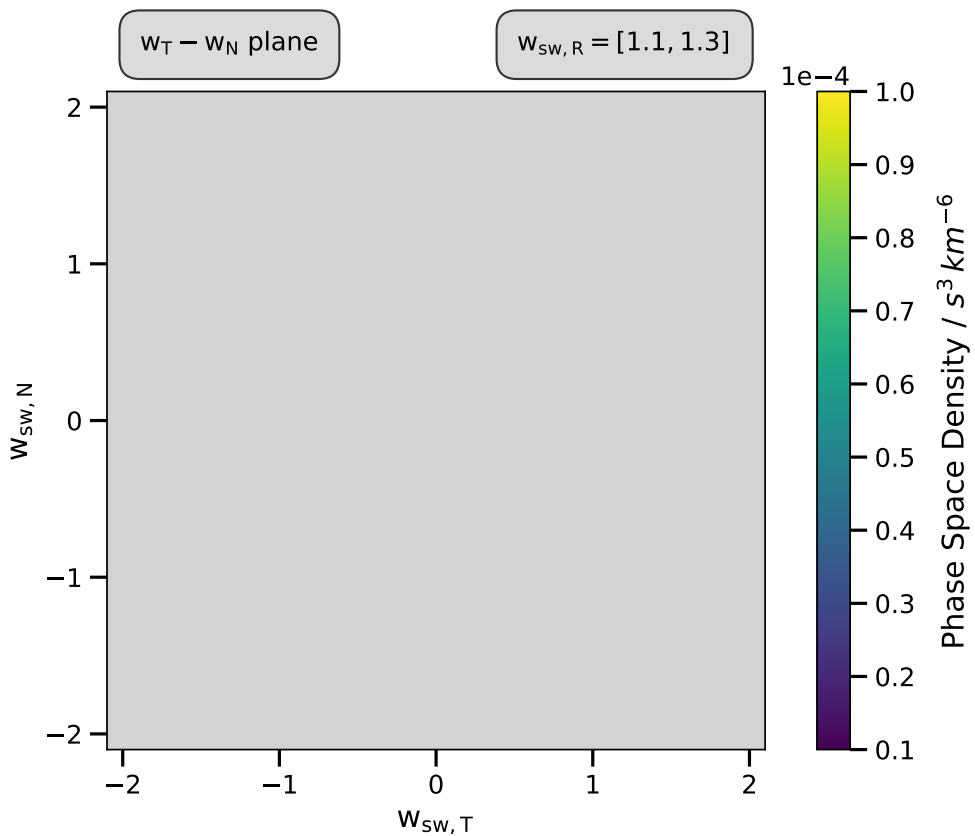
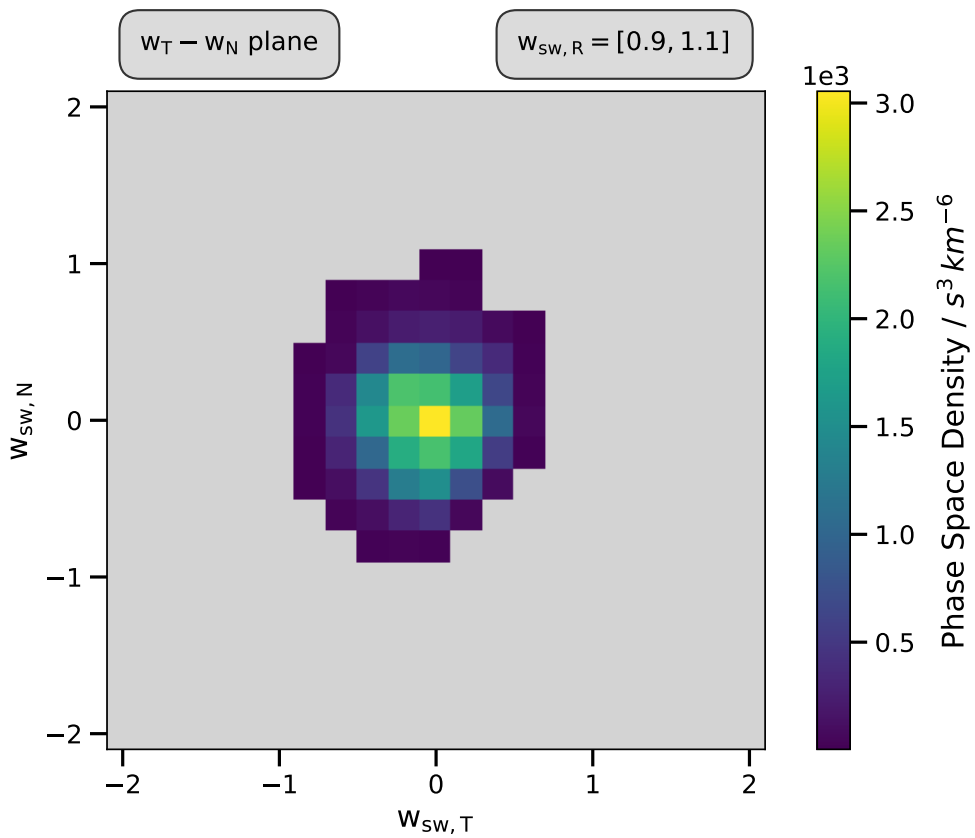
# PSD – Sequence













# Bibliography

- Allegrini, F., N. A. Schwadron, D. J. McComas, G. Gloeckler, and J. Geiss (May 2005). "Stability of the inner source pickup ions over the solar cycle". In: *Journal of Geophysical Research* 110.A5, A05105, A05105. DOI: [10.1029/2004JA010847](https://doi.org/10.1029/2004JA010847).
- Bame, S. J., D. J. McComas, B. L. Barraclough, J. L. Phillips, K. J. Sofaly, J. C. Chavez, B. E. Goldstein, and R. K. Sakurai (Jan. 1992). "The ULYSSES solar wind plasma experiment". In: *Astronomy and Astrophysics Supplement Series* 92.2, pp. 237–265.
- Berger, Lars (2008). "Velocity Distribution Functions of Heavy Ions in the Solar Wind at 1 AU". PhD thesis. Christian-Albrechts-Universität zu Kiel, IEAP.
- Drews, Christian, Lars Berger, Andreas Taut, Thies Peleikis, and Robert F. Wimmer-Schweingruber (Mar. 2015). "2D He<sup>+</sup> pickup ion velocity distribution functions: STEREO PLASTIC observations". In: *Astronomy & Astrophysics* 575, A97, A97. DOI: [10.1051/0004-6361/201425271](https://doi.org/10.1051/0004-6361/201425271).
- European Space Agency (2019). *ESA Website – Ulysses Orbit*. URL: <https://www.cosmos.esa.int/web/ulysses/the-ulysses-orbit> (visited on 10/27/2019).
- Fränz, M. and D. Harper (Feb. 2002). "Heliospheric coordinate systems. Corrected Version". In: *Planetary & Space Science* 50.2, pp. 217–233. DOI: [10.1016/S0032-0633\(01\)00119-2](https://doi.org/10.1016/S0032-0633(01)00119-2).
- Frisch, Priscilla C., Seth Redfield, and Jonathan D. Slavin (Sept. 2011). "The Interstellar Medium Surrounding the Sun". In: *Annual Review of Astronomy and Astrophysics* 49.1, pp. 237–279. DOI: [10.1146/annurev-astro-081710-102613](https://doi.org/10.1146/annurev-astro-081710-102613).
- Geiss, J., G. Gloeckler, L. A. Fisk, and R. von Steiger (1995). "C+ Pickup ions in the heliosphere and their origin". In: *Journal of Geophysical Research: Space Physics* 100.A12, pp. 23373–23377. DOI: [10.1029/95JA03051](https://doi.org/10.1029/95JA03051). eprint: <https://agupubs.onlinelibrary.wiley.com/doi/pdf/10.1029/95JA03051>. URL: <https://agupubs.onlinelibrary.wiley.com/doi/abs/10.1029/95JA03051>.
- Geiss, J., G. Gloeckler, and R. von Steiger (Apr. 1995). "Origin of the solar wind from composition data". In: *Space Science Reviews* 72.1, pp. 49–60. ISSN: 1572-9672. DOI: [10.1007/BF00768753](https://doi.org/10.1007/BF00768753). URL: <https://doi.org/10.1007/BF00768753>.
- Gloeckler, G., L. A. Fisk, J. Geiss, N. A. Schwadron, and T. H. Zurbuchen (Apr. 2000). "Elemental composition of the inner source pickup ions". In: *Journal of Geophysical Research* 105.A4, pp. 7459–7464. DOI: [10.1029/1999JA000224](https://doi.org/10.1029/1999JA000224).
- Gloeckler, G., J. Geiss, H. Balsiger, P. Bedini, J. C. Cain, J. Fischer, L. A. Fisk, A. B. Galvin, F. Gliem, D. C. Hamilton, J. V. Hollweg, F. M. Ipavich, R. Joos, S. Livi, R. A. Lundgren, U. Mall, J. F. McKenzie, K. W. Ogilvie, F. Ottens, W. Rieck, E. O. Tums, R. von Steiger, W. Weiss, and B. Wilken (Jan. 1992). "The Solar Wind Ion Composition Spectrometer". In: *Astronomy & Astrophysics Supplement Series* 92.2, pp. 267–289.
- Gloeckler, G., N. A. Schwadron, L. A. Fisk, and J. Geiss (Jan. 1995). "Weak pitch angle scattering of few MV rigidity ions from measurements of anisotropies in the distribution function of interstellar pickup H<sup>+</sup>". In: *Geophysical Research Letters* 22.19, pp. 2665–2668. DOI: [10.1029/95GL02480](https://doi.org/10.1029/95GL02480).
- Hunt-Ward, T. and T.P. Armstrong, eds. (1999). *Ulysses HISCALE Data Analysis Handbook*. Fundamental Technologies, LLC.

- Köten, Muharrem (Mar. 2009). "An improved efficiency model for ACE/SWICS - Determination of the carbon isotopic ratio  $^{13}\text{C} / ^{12}\text{C}$  in the solar wind from ACE/SWICS measurements". PhD thesis. Christian-Albrechts-Universität zu Kiel, IEAP.
- McComas, D. J., N. A. Schwadron, F. J. Crary, H. A. Elliott, D. T. Young, J. T. Gosling, M. F. Thomsen, E. Sittler, J.-J. Berthelier, K. Szego, and A. J. Coates (2004). "The interstellar hydrogen shadow: Observations of interstellar pickup ions beyond Jupiter". In: *Journal of Geophysical Research: Space Physics* 109.A2. DOI: [10.1029/2003JA010217](https://doi.org/10.1029/2003JA010217). eprint: <https://agupubs.onlinelibrary.wiley.com/doi/pdf/10.1029/2003JA010217>. URL: <https://agupubs.onlinelibrary.wiley.com/doi/abs/10.1029/2003JA010217>.
- Möbius, E., D. Hovestadt, B. Klecker, G. Scholer, and G. Gloeckler (1985). "Direct observation of He $^+$  pick-up ions of interstellar origin in the solar wind". In: *nature* 318 (6045), pp. 426–429. DOI: [10.1038/318426A0](https://doi.org/10.1038/318426A0).
- Möbius, E., D. Rucinski, M. A. Lee, and P. A. Isenberg (Jan. 1998). "Decreases in the antisunward flux of interstellar pickup He $^+$  associated with radial interplanetary magnetic field". In: *Journal of Geophysical Research* 103.A1, pp. 257–266. DOI: [10.1029/97JA02771](https://doi.org/10.1029/97JA02771).
- NASA HelioWeb (2019). *Heliocentric Trajectories for Selected Spacecraft, Planets, and Comets*. URL: <https://omniweb.gsfc.nasa.gov/coho/helios/heli.html> (visited on 06/01/2019).
- Oka, M., T. Terasawa, H. Noda, Y. Saito, and T. Mukai (June 2002). "'Torus' distribution of interstellar helium pickup ions: Direct observation". In: *Geophysical Research Letters* 29.12, 1612, p. 1612. DOI: [10.1029/2002GL015111](https://doi.org/10.1029/2002GL015111).
- Prölss, Gerd W. (2004). *Physik des erdnahen Weltraums. Eine Einführung*. Springer Berlin Heidelberg. DOI: [10.1007/978-3-642-18807-7](https://doi.org/10.1007/978-3-642-18807-7).
- Schwadron, N. A., J. Geiss, L. A. Fisk, G. Gloeckler, T. H. Zurbuchen, and R. von Steiger (Apr. 2000). "Inner source distributions: Theoretical interpretation, implications, and evidence for inner source protons". In: *Journal of Geophysical Research* 105.A4, pp. 7465–7472. DOI: [10.1029/1999JA000225](https://doi.org/10.1029/1999JA000225).
- Schwadron, N. A., E. Möbius, T. Leonard, S. A. Fuselier, D. J. McComas, D. Heirtzler, H. Kucharek, F. Rahmanifar, M. Bzowski, M. A. Kubiak, J. M. Sokół, P. Swaczyna, and P. Frisch (Oct. 2015). "Determination of Interstellar He Parameters Using Five Years of Data from the IBEX: Beyond Closed Form Approximations". In: *The Astrophysical Journal Supplement Series* 220.2, 25, p. 25. DOI: [10.1088/0067-0049/220/2/25](https://doi.org/10.1088/0067-0049/220/2/25).
- Stone, E. C., A. M. Frandsen, R. A. Mewaldt, E. R. Christian, D. Margolies, J. F. Ormes, and F. Snow (July 1998). "The Advanced Composition Explorer". In: *Space Science Reviews* 86, pp. 1–22. DOI: [10.1023/A:1005082526237](https://doi.org/10.1023/A:1005082526237).
- SWICS DPU (1988). Ed. by F. Gliem, W. Rieck, and H. Dinse.
- Ulysses Final Archive (2008). Ed. by European Space Agency. URL: <http://ufa.esac.esa.int/ufa/#data> (visited on 08/01/2019).
- Vasyliunas, V. M. and G. L. Siscoe (1976). "On the flux and the energy spectrum of interstellar ions in the solar system". In: *Journal of Geophysical Research (1896-1977)* (7).
- Wenzel, K. P., R. G. Marsden, D. E. Page, and E. J. Smith (Jan. 1992). "The ULYSSES Mission". In: *Astronomy and Astrophysics Supplement* 92, p. 207.
- Wimmer-Schweingruber, R. F. and P. Bochsler (May 2002). "On the Origin of Inner-Source Pickup Ions". In: *Geophysical Research Letters* 30.2, pp. 49-1 - 49-4.

# Eidesstattliche Erklärung

Hiermit erkläre ich, dass ich die vorliegende Masterarbeit selbstständig und lediglich unter Benutzung der angegebenen Quellen und Hilfsmittel verfasst habe. Ferner versichere ich, dass die vorliegende Arbeit noch nicht im Rahmen eines anderen Prüfungsverfahrens eingereicht wurde.

Ort, Datum:

Unterschrift:



# Danksagung

The acknowledgments and the people to thank go here, don't forget to include your project advisor...